Investigation of Atmospheric Trace Gas Composition and Air-Sea Flux Detection Potential over Halifax (NS) Harbour Using OP-FTIR Spectroscopy

By
Lukas Donovan

A Thesis Submitted to
Saint Mary's University, Halifax, Nova Scotia
in Partial Fulfillment of the Requirements for
the Degree of BSc Honours Physics

April, 2024, Halifax, Nova Scotia

Approved:	Dr. Aldona Wiacek Supervisor
Approved:	Dr. Malcolm Butler Reader
Date:	April 30, 2024

Investigation of Atmospheric Trace Gas Composition and Air-Sea Flux Detection Potential over Halifax (NS) Harbour Using OP-FTIR Spectroscopy

By
Lukas Donovan

A Thesis Submitted to
Saint Mary's University, Halifax, Nova Scotia
in Partial Fulfillment of the Requirements for
the Degree of BSc Honours Physics

April, 2024, Halifax, Nova Scotia

Approved:	Dr. Aldona Wiacek Supervisor
Approved:	Dr. Malcolm Butler Reader
Date:	April 30, 2024

Investigation of Atmospheric Trace Gas Composition and Air-Sea Flux Detection Potential over the Halifax (NS) Harbour Using OP-FTIR Spectroscopy

By Lukas Donovan

Abstract

In a world where air quality and the future of the earth are being heavily influenced by anthropogenic pollution, it is vital to protect air quality and improve our understanding of the relationship between the ocean and atmospheric trace gas composition. Tropospheric trace gas concentrations as well as vertical concentration differences (an input to the calculation of ocean-air flux) are derived over a period of one month (August – September, 2021), based on available long Open-Path Fourier Transform InfraRed (OP-FTIR) spectroscopic measurements at the air-sea interface in ambient air in Halifax, NS. Average concentrations and measurement errors are reported, as well as possible explanations driving the temporal behaviour of key air-quality related trace gases (ammonia, formic acid, carbonyl sulfide, carbon monoxide, and methanol), as well as the greenhouse gas carbon dioxide. The concentration results show ship plume events as well as diurnal cycles. The concentration differences suggest an ocean source of carbonyl sulfide and formic acid, and an ocean sink of carbon dioxide and ammonia, which is consistent with prior knowledge of air-sea gas exchange. This is the first report of the flux-related concentration difference of these gases in a marine environment by this technique. Prior to these spectral retrievals, the sensitivity to different parameter choices in fitting OP-FTIR spectra using the Multiple Atmospheric Layer Transition (MALT) Non-Linear Least Squares (NLLS) algorithm was investigated, with a focus on the FOV parameter, which is related to the optical configuration of the spectrometer and spectral line broadening.

April 30, 2024

Acknowledgements

Thank you to my family for all their support over the years.

Thank you to Dr. Aldona Wiacek, my supervisor, for her support and encouragement throughout.

Thank you to the members of the Wiacek Atmospheric Research Group for their support and inspiration as well.

Thank you to Dr. Malcolm Butler for being my reader and giving me valuable feedback on my work.

Table of Contents

1. Introduction

1.1 – Motivation: Target Molecules and the Environment

State-of-the-art global earth system models, which increasingly include biogeochemical processes, currently have large uncertainties on their simulated ocean-air fluxes of trace gases. The ocean is known to be a source, sink, or both, of various trace gases, and is in some cases a dominant factor in the resultant composition of the atmosphere. As the climate of the Earth changes, so does the nature of ocean-air interactions, and it is important to increase scientific knowledge of these processes to improve our predictive capacity — both for present and future climate predictions. The list of target molecules investigated in this work contains greenhouse gases (GHGs) (carbon dioxide (CO_2)), air quality (AQ) related pollutants like carbon monoxide (CO), ozone (O_3), ammonia (NH_3), and Volatile Organic Compounds (VOCs).

Also imperative for environmental preservation is the effective creation of policies that restrict destructive human activity. For example, Wiacek et al. (2018) showed that passenger ships (cruise ships) are responsible for almost 20% of trace gas and aerosol emissions during cruise ship season in Halifax. It is immediately worth mentioning that these emissions are a detriment to not only the environment and affected ecosystems but also to human health. Wiacek et al. also showed that shipping emissions from the Halifax port were "greater than or comparable to all vehicle NO_X emissions in the city" over one year. This project similarly aims to demonstrate the ability of the Open-Path Fourier Transform Infrared (OP-FTIR) technique to detect shipping-related AQ-degrading trace gas emissions. With subsequent analysis, this information can be used to improve policies

in the shipping sector, as well as to identify and prevent the perpetuation of harmful practices.

Atmospheric processes are complex; acids, bases, and the aerosolized salts that they form are strongly coupled to cloud formation — the largest unknown in climate modeling because of its strong influence on the radiative balance of the Earth. Acids and bases also cause ocean acidification and eutrophication, respectively. NH_3 is the most prominent atmospheric base involved in particulate matter formation, by combination with acids to make salts (Behera et al., 2013). The environmental role of NH_3 is even more complex as it donates both H^+ and nitrogen to ecosystems following deposition, acting as both an acid and a fertilizer, and contributing to harmful ocean phenomena such as algal blooms and hypoxia. These in turn lead to greenhouse gas (N_2O) emissions from the ocean to the atmosphere. OCS is another target molecule of this study because it is the main sulfur-containing compound in the atmosphere, maintaining natural sulfuric acid and sulfate aerosol production, important in cloud formation and in maintaining the globally cooling stratospheric aerosol layer. The complexity of the chemical family of VOCs strongly related to AQ is such that it includes hundreds of species that participate in thousands of chemical reactions; this study analyzes only the concentration of the VOCs methanol (CH_3OH) and formic acid (HCOOH), which participate in harmful tropospheric ozone and secondary organic aerosol formation (HCOOH is both a VOC and an important organic acid).

The main target molecules of this study with expected ocean-air fluxes are OCS, NH_3, HCOOH, and CO_2 (CH_3OH has a known ocean sink, but was not pursued due to

time constraints). This project investigates the potential to detect ocean-air flux from the vertical concentration gradients of molecules in the atmosphere measured by the OP-FTIR 'flux-gradient' technique. This approach has been used only once before at the air-sea interface for the GHG nitrous oxide (N_2O) (Hellmich, 2022), and is based on the land-air gas flux work of Flesch et al. (2016). This is a novel technique with which to measure the ocean-air flux of trace gases, with high temporal resolution and the capacity to detect a large variety of molecules simultaneously, provided they absorb infrared light at sufficient levels. These capabilities are unique to the OP-FTIR sensing method. Typical methods for ocean-air flux measurements such as eddy covariance (e.g. Miller et al., 2010) are more commonly used but not as versatile. Previous studies using these other techniques have found that NH_3 has an expected ocean sink at the latitude of Halifax (Paulot et al., 2015), OCS has an expected source in the ocean (e.g. Lennartz et al., 2020; Ferek & Andreae, 1984), and atmospheric HCOOH has a missing source that may be due to ocean-air flux (HCOOH is also formed via photochemical processes in the atmosphere) (Millet et al., 2015). CO_2 has been found to have an ocean uptake of ~ 1 mol/m^2/year around Nova Scotia (PMEL Carbon Program, 2000) and the ocean absorbs 25% of anthropogenic CO_2 emissions at all times (Watson et al., 2020), mitigating the atmospheric concentration increase by doing so.

1.2 – Overview of OP-FTIR Spectroscopy and Spectral Fitting Methodology

Spectroscopy is the study of electromagnetic radiation emission or absorption by matter. In OP-FTIR spectroscopy, a beam of infrared light is generated and transmitted through an open atmospheric path of several hundred meters, then a Fourier Transform (IR) spectrometer is used to measure the IR absorption signals (i.e., the absorption spectra) due to the IR-absorbing gases in the open path (the geometry of the experimental setup is discussed in the next section). In order to 'retrieve' the concentrations of the absorbing atmospheric trace gases, the spectra recorded by the OP-FTIR spectrometer are fitted using the program 'MALT' (Griffith, 1996) in this study, which currently uses a Non-Linear Least Squares (NLLS) approach for spectral fitting and does not assume linearity of Beer's Law (Griffith, 2010). The original version of MALT used Classical Least Squares (CLS) fitting (Griffith, 1996) and assumed linearity in Beer's Law (transmitted radiation intensity, I, is proportional to the absorber concentration, C). Beer's Law is fully stated as $\log_{10}(I_o/I) = A\ (= \varepsilon bC)$ in which the absorbance, A, of IR light is related to gas concentration, C, with constants ε and b representing the molar absorptivity and the path length, respectively; I_o represents the initial radiation intensity before attenuating matter is encountered. The NLLS 'retrieval' process consists of iteratively simulating the spectrum with varying gas concentrations so as to minimize a cost function derived from the difference between the simulated and measured spectrum. This simulation allows for a deconstruction of the recorded spectrum into the contributions (i.e. absorption signatures, or spectral absorption lines) of the various gases present in the beam path of the spectrometer (see Figures 1-1 & 1-2 for an example of

this). This can be done using the HITRAN spectral database (e.g. HITRAN 2004 (Rothman et al., 2005)), which is based on both first principles calculations and high-precision laboratory measurements of the vibrational and rotational state transitions of molecules (e.g., line strength and position (wavenumber)); see, e.g., *Fundamentals of Molecular Spectroscopy* by Banwell and McCash (1994) for a more in-depth overview of the theory. The forward model of MALT (for simulating the gas spectrum) can also be run using a reference spectrum from the Pacific Northwest National Laboratory (PNNL) database (Sharpe et al., 2004) instead of the HITRAN database. The spectral transmission model also depends on continuum, instrumental and environmental parameters. The continuum parameters used were 'poly2' and 'poly3' (relating to the degree of the fitted polynomial used to describe the spectral continuum; 'poly2' = first degree polynomial with two terms, and 'poly3' = second degree polynomial with three terms — this is the convention used by MALT). Although it is possible to fit higher order polynomials, it was sufficient to consider these two options for this project's purposes due to the relatively simple nature of the relevant spectral continuums — mainly because the fitting process focused on smaller spectral regions (in which the section of the continuum to be modelled is less complex) where the specific absorption features of a target molecule are found. The instrumental parameters modelled were phase, shift, effective apodization (FAP), and field of view (FOV). They relate to the details of an FTIR spectrometer and manifest in the spectrum as an asymmetry of all lines (phase), a shift of all lines, and a line broadening/line shape adjustment of all lines (FAP and FOV). Finally, the environmental parameters are atmospheric pressure and temperature, which influence

both line strength and line broadening coefficients calculated based on the HITRAN database. An example of this method in practice for a very low abundance gas (ammonia) is illustrated in Figure 1-1 and Figure 1-2. Examples showing the targeted absorption features for the other molecules retrieved in this work can be seen in Appendix – A.1.

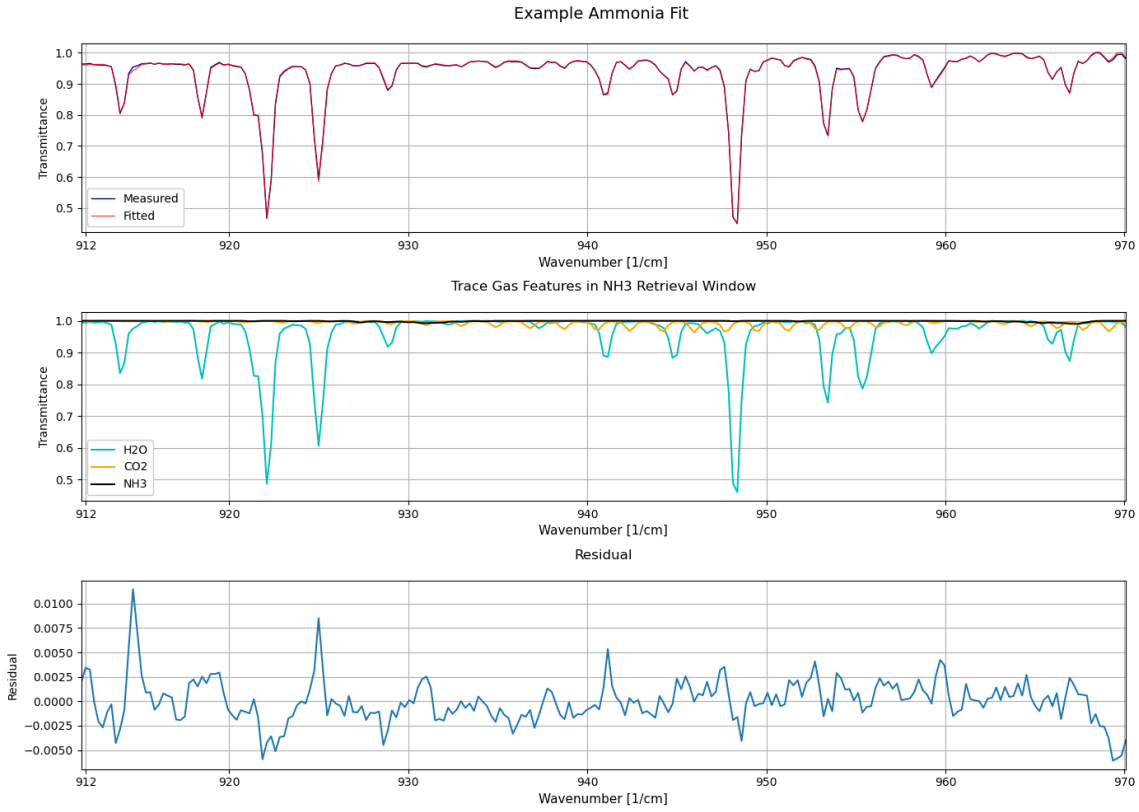

Figure 1-1: Example of an ammonia spectral fit in the 912 – 970 cm^{-1} region. The top panel shows the measured vs simulated (fitted) spectrum, the middle panel shows the 'decomposition' of the spectrum into the contributions from each gas absorption, and the bottom panel shows the residual spectrum (fitted – measured).

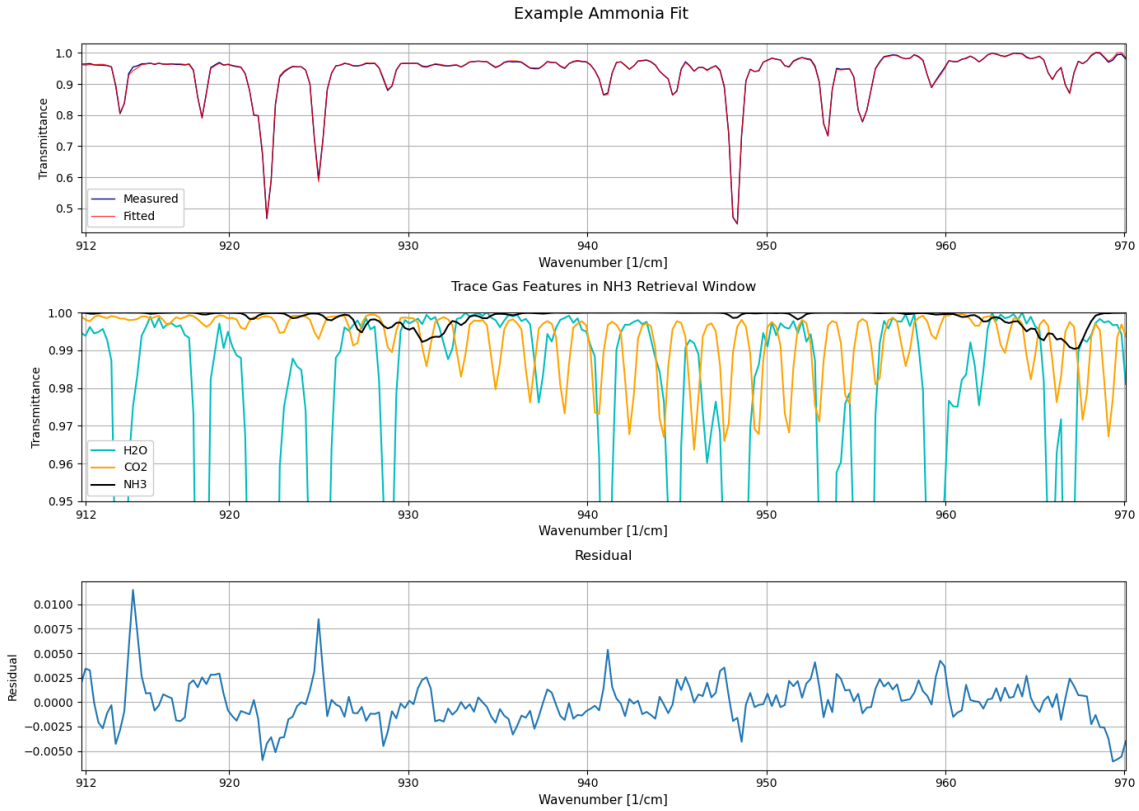

Figure 1-2: Figure 1-1 zoomed in to show the shallow NH_3 absorption feature in this window.

1.3 – Objectives, Organization of Thesis and Scope of Work

The aim of this project was to derive the atmospheric concentrations of the previously mentioned trace gases by performing spectral fitting on OP-FTIR data taken at the Department of National Defense (DND) in Halifax (four weeks spanning August – September, 2021). The open-path data consists of two datasets (series 1 and 2) recorded at a known vertical separation above and across the Halifax harbour, and so in addition to gas concentration time-series analysis, this project investigates the potential to detect ocean-air flux for the targeted gas molecules following the procedure of Hellmich (2022),

which is possible to derive from the vertical concentration gradient. Figure 1-3 shows the geometry of the experimental setup. The air-sea flux-related concentration gradient results represent the furthest level of data processing and are therefore presented last (Section 3.4), alongside noteworthy observations regarding the general behaviour of these target molecules. The concentration time series results used to study shipping emissions (based on time-correlated increases in pollutant concentrations) logically fall in Section 3.3, since they are one data processing step below the concentration gradient results. Prior to these one-month spectral retrievals, the parameters used for fitting spectra with the program MALT were examined based on an extensive assembly of short-term (24-hour) NH_3 retrievals (work that began over summer 2023) as well as joint CO and CO_2 retrievals (in one spectral window), with the goal of determining what makes a fitting configuration systematically robust. This knowledge was then generalized and applied to the retrievals for the other gases.

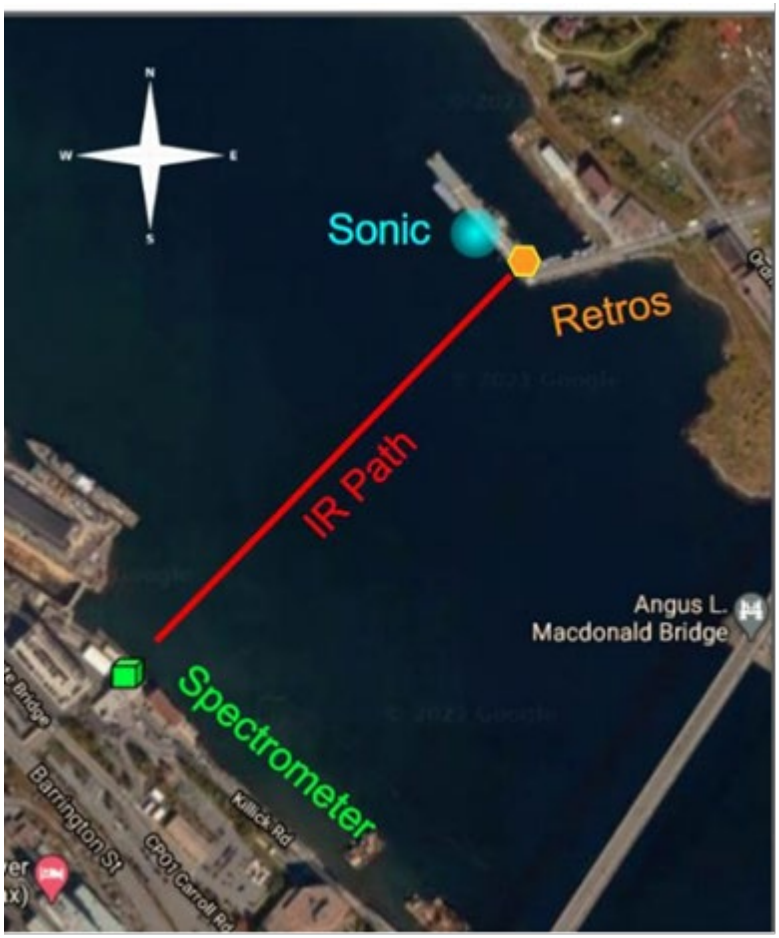

Figure 1-3: Experimental setup. Adapted from Hellmich (2022). Infrared radiation is continuously generated at the spectrometer, traverses the open path to the retroreflectors (alternating continuously between the top height and the bottom height), which reflect it back to the spectrometer, where a detector is co-located and an absorption spectrum is recorded. A 3-D sonic anemometer was deployed outside of the period studied in this work (i.e., from Dec 2020 to May 2021).

Originally, the investigation into spectral fitting parameters was going to be a small component of the Honours research, assuming that this work would be completed during summer 2023. However, understanding the fitting process is a complex task since it is not completely generalizable from one gas to another. As general curiosity regarding the accuracy, sensitivity, and nature of OP-FTIR spectral retrievals grew over time, the

decision was made to invest more time into optimizing the retrievals. So, in addition to analyzing the effect of fitting/fixing various spectrometer-related parameters (phase, shift, effective apodization (FAP), field of view (FOV)) for NH_3 (much of which was done during summer 2023), the same analysis was expanded and repeated for CO and CO_2 (which were co-retrieved from the same spectral region) to see how various sensitivities (e.g., how the retrieved concentration varies with respect to fit parameters used) compared for gases with stronger spectral absorption features (CO and CO_2) versus for weak absorbers (NH_3). This work is chronologically presented in Section 3.1, as it represents a broad investigation that influenced much of the rest of this work. Further analysis of the FOV parameter was inspired by Smith et al. (2011), who found (via CO and other gas retrievals) that an optimal initial FOV value (FOV is important since it is convolved with the line shape of each absorption feature during the spectral simulation) was 10% different from the value stated by the spectrometer manufacturer. They also showed that this relatively small difference in initial FOV value could increase the true error in CO and other gases (w.r.t. a known sample concentration) from ~ 0 to 15%, while the reported MALT NLLS algorithm retrieval error was far less sensitive. They also showed that CO absorption lines were most sensitive to the instrument line shape (ILS) due to their narrow nature (more narrow than CO_2 and NH_3) and are thus a good candidate for fitting the true FOV. To investigate this for our own spectrometer, CO and NH_3 were fitted in ~1 month of data (August – September, 2021), both with and without FOV being allowed to vary with each fitting iteration. Two additional retrievals were done for NH_3 (one fixed FOV, one fitted FOV) using the average fitted FOV from the CO

retrieval as an initial input FOV, to determine whether this approach performed better in the retrieval of a weakly-absorbing gas. This detailed analysis of two related retrieval parameter effects and interactions is presented in Section 3.2.

Before Results, the Methods section details the spectral fitting parameter choices study (2.1), data quality control and filtering for both concentration time series and concentration differences (2.2), concentration time series analysis steps (2.3), and the vertical air-sea flux-related concentration gradient analysis (2.4). The Discussion is again divided into results pertaining to retrieval parameter choices (4.1) and concentration time series and gradients (4.2). The Conclusions section includes an outline of future work, while Appendices 1-6 document several supplementary plots and interesting but non-central findings.

This thesis makes use of OP-FTIR absorption spectra collected by the Wiacek Atmospheric Research Group in 2020-2021. All retrievals and analyses presented in this thesis were carried out independently by the author, with regular input from the Supervisor (Dr. Wiacek) and the one-time input of a Second Reader (Dr. Butler). All figures were created independently by the author, unless otherwise noted. Finally, this work involved porting a large and complex MATLAB code for retrievals into Python (Section 2.3), which is available as a digital resource, upon request.

2. Methods

2.1 – Sensitivity Analysis of Spectral Fitting Parameter Choices

To analyze the effect of fitting or fixing instrumental and spectral continuum parameters in the forward model (i.e., determining whether allowing them to vary in the iterative fitting algorithm strongly affects the retrieval results), an extensive set of different retrieval configuration experiments was run on the 24-hour data set (N = 360 spectra) selected as described in Section 2.2. The retrieval performance of each parameter combination was described by two metrics: a single fit RMS (root mean square) residual value over the spectral window for each fit, and the percent error reported by the MALT NLLS algorithm on each retrieved concentration of the target molecule. This analysis mainly focused on NH_3 and was done for every possible combination (25 total) of the instrumental parameters 'poly2', 'poly3', 'phase', 'shift', FAP, and FOV (fixed or fitted). Additionally, three fit combinations tested the updated HITRAN 2020 H_2O spectroscopy (updated as of July 21, 2023) from the SFIT4 version 1.0.xx release notes (Hannigan, 2023), and were labelled 'HIT20' (water is the most abundant trace gas and has pervasive spectral signatures, therefore improvements in line parameters can lead to significant improvements in spectral fits). This multitude of fit configurations was plotted in the variable space of reported MALT retrieval error vs. RMS residual, where both were averaged over the 360 individual fits for a given configuration, to look for an optimal retrieval parameter combination that (ideally) minimized both, or simply to identify parameters that are ubiquitous in 'good' fits. These fit configurations were also repeated using a PNNL reference spectrum for NH_3 to investigate the difference between using

HITRAN and PNNL. Although HITRAN is known to be a better database for absorption parameters (since it is based on first-principle calculations and ultra-high precision lab measurements), there are many gases which are absent from the HITRAN database (their 'line-by-line' calculations are too complex) for which it is necessary to use a PNNL reference 'cross-section' spectrum (e.g. acetic acid and acetaldehyde). Given this, it is informative to quantify how different retrieval results may be when using these two databases for a gas which can be retrieved using both (assuming that differences for NH_3 translate to differences for other gases). The 24-hour retrievals for the NH_3 sensitivity analysis (Section 3.1.1) were mostly done during the summer of 2023 in the same spectral region of 1078 – 1125 cm^{-1} (Appendix A.1, Figure A-7), with H_2O and CO_2 as interferers. This window turned out to be suboptimal for NH_3 retrievals upon further examination in fall 2023, when a superior window was found and used to fit the entire one-month dataset for this Honours work (Sections 3.3 and 3.4, which focus on concentration and flux-related time series). A subsequent investigation focusing directly on the FOV parameter was done (Section 3.2), testing whether NH_3 and CO would have a 'better' fit with a fixed or fitted FOV; this was done in the superior NH_3 window mentioned above due to better absorption features (912 – 970 cm^{-1}), with the same interferers (H_2O and CO_2). For the CO component of the investigation, CO was in all cases fitted with H_2O and CO_2 as interferers in the spectral region of 2080 – 2133 cm^{-1}. The spectral windows and retrieval configurations used for each gas are summarized in Appendix A.2, Table A-2, with examples of spectral fits shown in Appendix A.1.

This work also tested whether setting the initial FOV value (and leaving it fixed during fitting) to the average fitted value from CO fits would improve NH_3 fit quality. This hypothesis was based on the fact that CO is more sensitive to the ILS convolution due to its narrow absorption lines, and also has strong absorption features, meaning it contains sufficient information on the true FOV and is thus a good fit from which to estimate FOV for fixed use in the NH_3 retrieval (Smith et al., 2011), as introduced in Section 1.2. To better characterize the effect of fitting or fixing FOV, separate retrievals of both CO and NH_3 were performed with FOV fixed or fitted in order to compare fit metrics (i.e., RMS residual, % retrieval error, average concentration and standard deviation in time, etc.). Both retrievals also fitted phase, shift, and FAP, i.e., physically justified parameters related to spectral line asymmetry, wavenumber shift and line broadening. Finally, incorporating the retrieved FOV from the CO retrieval as the initial FOV value, two more retrievals of NH_3 were performed (one fixing FOV, one fitting FOV) to determine whether the theoretical FOV was incorrect and leading to inferior retrievals.

2.2 – Spectral Data Quality and Filtering

Ambient environmental factors influence the quality of spectral data, and they are recorded in parallel with spectral information: pressure, temperature, relative humidity (RH), solar intensity, UV intensity, wind direction and speed, and precipitation. The source of this data is the Davis Weather Station at Halifax Harbour, nearly co-located

with the Sonic anemometer shown in Figure 1-3. Figure 2-1 shows the weather data that was used to identify a day containing high signal-to-noise ratio (SNR) spectral data, which is most likely to occur on fair-weather, low humidity days. Based on this, August 15th (2021) was selected for the study on fitting parameter choices (Section 3.1). Figure 2-2 shows the weather data for this day; the bottom right panel shows a symmetric solar intensity curve (cloudless conditions), and the third panel down on the left side shows a daytime minimum in RH, with no precipitation (third panel down on right), all indicators of high quality spectral data. Wind speeds are not at a minimum, but at 6 m/s they are reasonable. Some retrievals failed to run and returned RMS values of 'NaN' (Not a Number) leading to static concentration values (i.e. simply the initial 'guess' value); these fits were removed from the dataset as well. These retrievals were caused by a lack of corresponding temperature/pressure data, essential inputs for the spectral simulation, which can be seen as missing values in Figure 2-2.

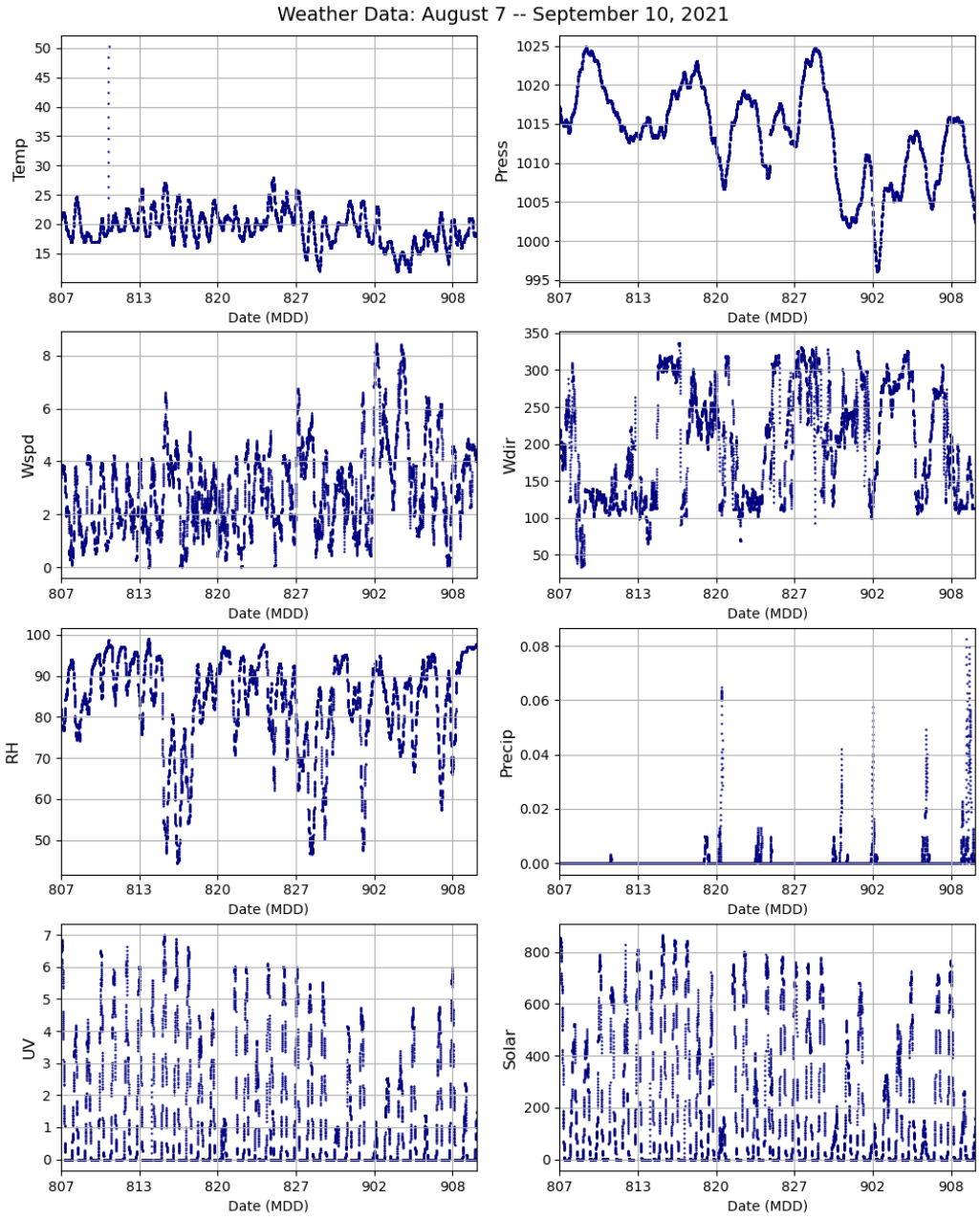

Figure 2-1: Weather data over the one-month time period (08/07/2021 – 09/10/2021). Units are: temperature ('Temp') in °C, pressure ('Press') in mbar, wind speed (Wspd) in m/s, wind direction ('Wdir') as an angle between 0 and 360 degrees, relative humidity ('RH') as a percentage, precipitation ('Precip') in mm, UV as the typical UV index, and solar radiation in W/m^2.

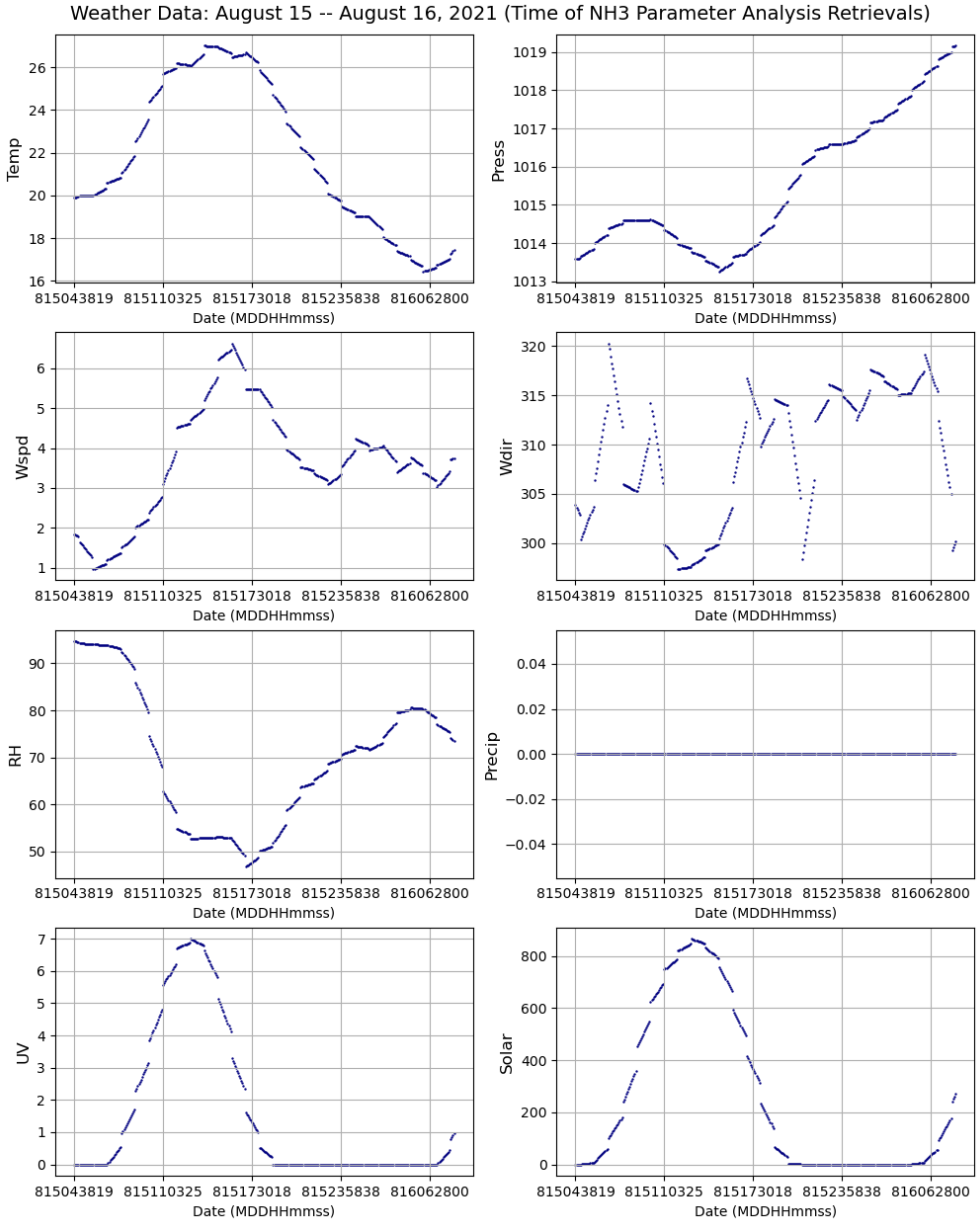

Figure 2-2: Same as Figure 2-1, but zoomed in to show weather data for the day used for the NH_3 and CO fitting parameter analysis.

It is common practice to filter spectral data based on IR signal levels at 2500 cm^{-1} (signal intensity > 0.05 a.u.), which in this case removed ~8.3% of data points (for both series 1 and series 2); this approach helps remove visible outliers from the concentration data. We

can see in Figure 2-3 that outliers are produced in areas of lower signal intensity (e.g. highly scattered CO concentrations, and also negative retrieved concentrations that are unphysical), which correspond to instances of high retrieval RMS residual (Figure 2-4). The cut-off value of 0.05 a.u. was determined by trial and error, until a minimum signal intensity that effectively removed the noisy/unphysical concentrations was found. The same time series is shown in Figures 2-3 – 2-6, coloured by the signal intensity and RMS residual before and after filtering the data.

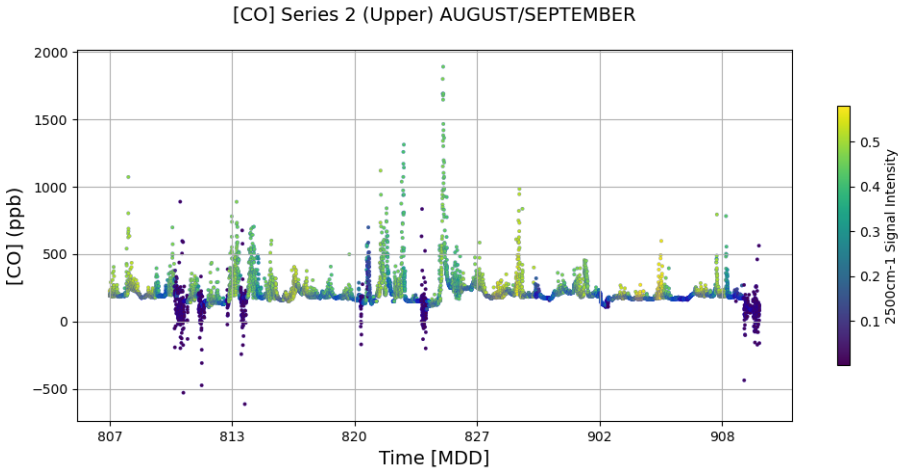

Figure 2-3: Unfiltered concentration time series for CO, coloured by 2500 cm^{-1} signal intensity.

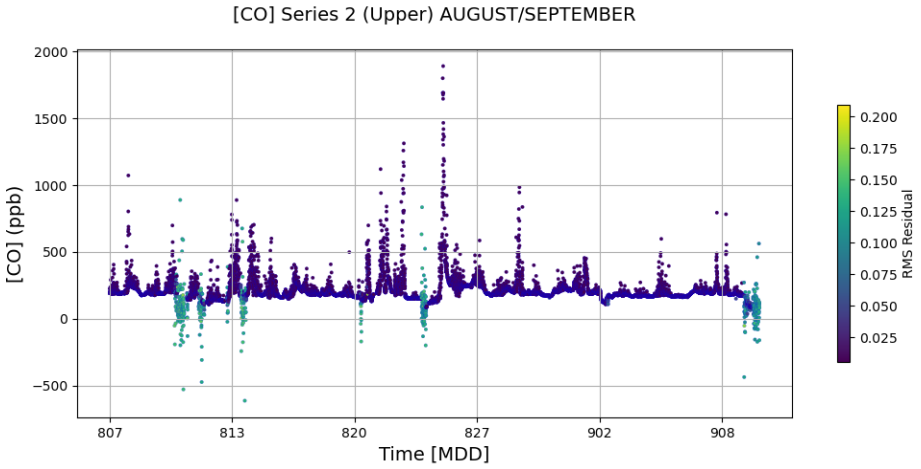

Figure 2-4: Unfiltered concentration time series for CO, coloured by retrieval RMS residual.

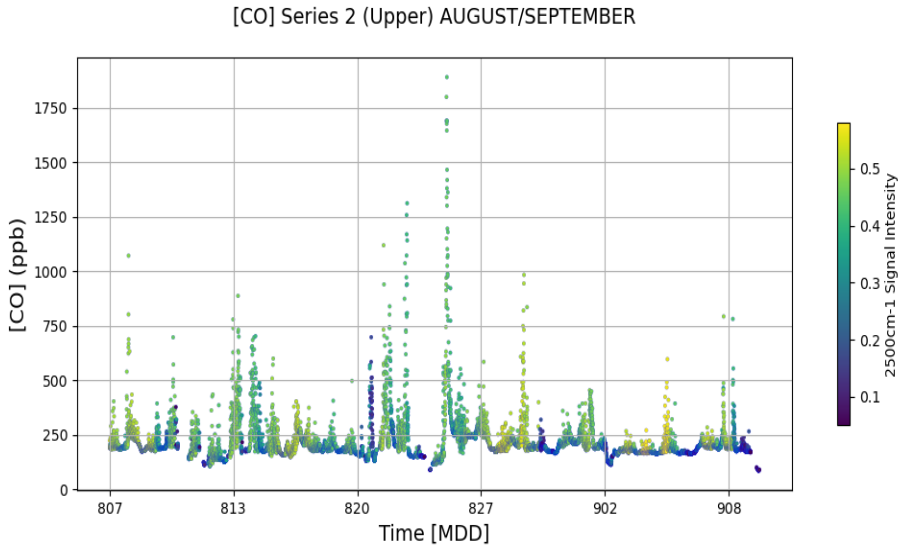

Figure 2-5: CO concentration time series after filtering the data based on the following criteria: 2500 cm^{-1} signal intensity > 0.05 a.u., and RMS ≠ NaN.

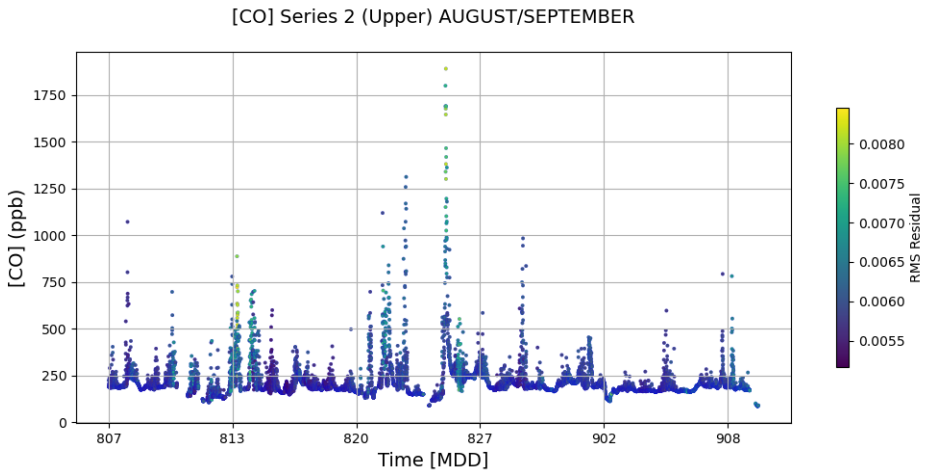

Figure 2-6: Same as Figure 2-5 but coloured by RMS Residual instead of signal intensity.

As mentioned above, the RMS residual NaN values were found to correspond to spectra which did not have associated temperature measurement data (a key input to MALT as it largely determines spectral lineshape), and so the program failed to run correctly. There were 216 spectra with this problem, and the total number of points removed after both signal intensity and NaN filtering was:

- N = 1041 removed for series 1 (total)
- N = 1037 removed for series 2 (total)

so that ~ 9% of the data set was removed for each series in total. For reference, a plot of 2500 cm^{-1} signal intensity was created for series 2 during the time period used in this study (Figure 2-7). Precipitation and fog events correspond to regions of greatly reduced IR signal intensity and can be anti-correlated with the high (near 100%) RH and precipitation values in Figure 2-1. The ~24h period on which the parameter analysis was

done is identified between the x-axis ticks labelled ‘815’ and ‘816’, a date with relatively good signal intensity and sunny and stable weather conditions (August 15th, 2021).

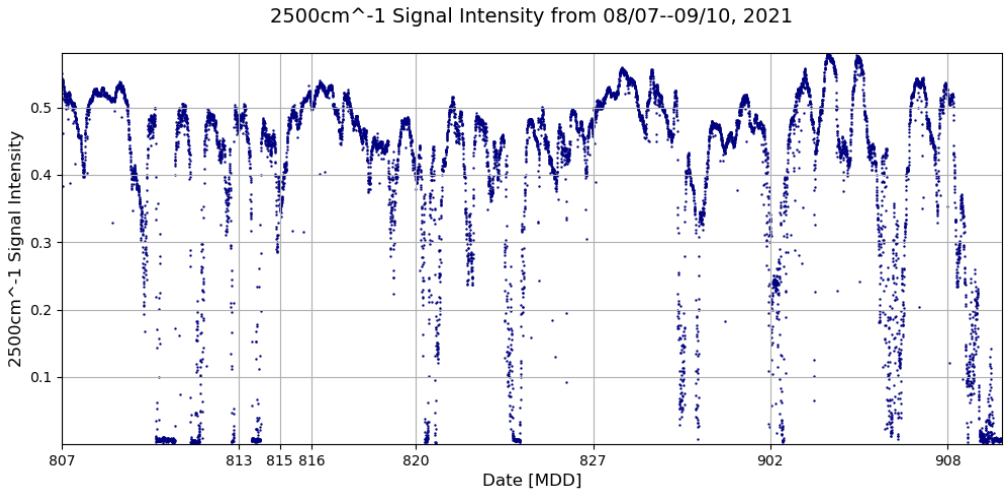

Figure 2-7: Upper path (series 2) IR Signal intensity from 08/07–09/10 (2021).

2.3 – Trace Gas Concentration Retrieval Execution and Analysis

The individual MALT retrievals of concentration from each spectrum are run using a ‘shell’ code that supplies and directs input and output text files. As part of this work, this code was translated and improved from a set of MATLAB scripts developed by Dr. Li Li in the Wiacek Atmospheric Research Group, and then implemented in Python using object-oriented programming (summer 2023). After assembling retrieval data and filtering it as described in section 2.2, gas concentrations were plotted over the entire one-month period, as well as over daily time scales to identify smaller scale temporal variations in gas concentrations or (vertical) concentration differences. Plots

over smaller time scales were coloured by solar radiation intensity to indicate whether sunlight was a factor in trace gas behaviour (i.e. temporal variation) via photochemical reactions.

2.4 – Ocean-Air Flux Related

The approach for using a vertical concentration difference, ΔC, to derive a flux rate is based on the land-air gas flux work of Flesch et al. (2016) and follows that of Hellmich (2022), demonstrated for N_2O in Halifax Harbour. The concentration data was not interpolated before subtraction to avoid additional error, deemed acceptable since the time separation between concentration time series is small (~2 min between the middle of acquisition of each spectrum). This project focuses on estimating the signal to noise ratio for the vertical concentration difference of target gases that are expected to demonstrate ocean-air flux. The calculated concentration difference was plotted over the time range of the retrievals, including MALT errors which were propagated through the subtraction using the formula for gaussian error propagation: $\sigma_{\Delta C} = \sqrt{{\sigma_{C1}}^2 + {\sigma_{C2}}^2}$, in which the subscripts C1 and C2 indicate series 1 and series 2 concentrations. These errors help identify where the concentration difference may be significant given the uncertainty. The concentration differences were also binned by 30 minutes (and in some cases 3 hours) following the procedure of Hellmich (2022) to observe the variation in ΔC on different temporal scales as well as to convert the uncertainty into standard error (calculated from the standard deviation over 30 minutes divided by $\sqrt{N = 7}$, based on the fact that there

are ~7 spectra recorded for each series in 30 minutes, each taking ~2 min and alternating between series 1 and 2), assuming flux to be stable over this time range. This standard error does not make use of the MALT retrieval error, and instead captures the variation in the repeated measurement of an assumed-to-be constant quantity during a 30-minute window; this approach provides an estimate of the measurement stability that may be more directly related to measurement precision than the MALT retrieval error is.

3. Results

3.1 – Sensitivity Analysis of Spectral Fitting Methodology

3.1.1 – Ammonia (NH_3)

It was initially thought that plotting the results from each fitting configuration (described in more detail below) for HITRAN and PNNL NH_3 retrievals in a parameter space of average % Retrieval Error vs average RMS residual (Figure 3-1) would yield a clearly optimal fitting configuration, along with the expected result of HITRAN line-by-line spectral line calculations out-performing the PNNL reference spectrum method. This was not however the case, and instead called for a deeper understanding of the MALT NLLS algorithm and the fitting parameters used.

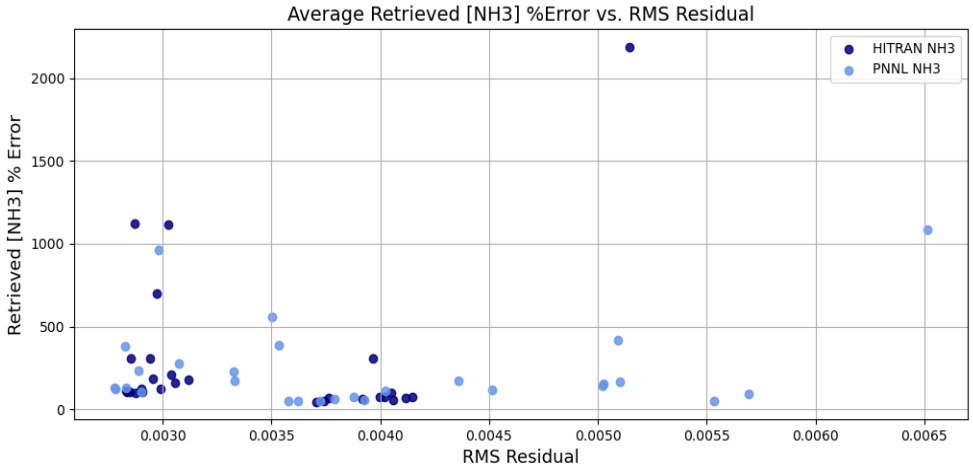

Figure 3-1: Average values (based on 360 spectra in a 24-hour period) for percent error on the target molecule's retrieved concentration (NH_3) vs. the RMS residual of the spectral fit. There are 28 retrieval parameter combinations, doubled by using either a PNNL reference spectrum or the HITRAN line-by-line database for NH_3.

Figure 3-1 shows that rather than HITRAN clearly performing better, there are many retrieval combinations using the PNNL database that lead to lower RMS residual

and retrieval error pairs. Notably, PNNL leads to many higher RMS residual values, but its retrieval error is on par with HITRAN retrieval error (It is noteworthy that retrieval errors are normally high for NH_3 (~100% in some cases) because it is a very low abundance gas, pushing the technique to its limit). To better compare the effect of PNNL vs. HITRAN in each of the 28 retrieval cases, a HITRAN – PNNL difference plot was made for both RMS residual and retrieval error (Figure 3-2). Although there appears to be no obvious category of fits for which PNNL out-performed HITRAN, it is interesting that it happened at all. The common characteristic of fits where HITRAN outperforms PNNL is that none of them include the intrinsic line broadening parameter FOV (only the second-order broadening parameter FAP); without FOV it is perhaps more difficult for the inferior PNNL spectral database to lead to a small RMS residual. The most extreme change in retrieval percent error (where HITRAN retrievals had the bigger error) corresponds to a fit with only the poly2 parameter but no phase, shift or either line broadening parameter (FOV and FAP), which is a ‘very rough’ way to fit a measured spectrum.

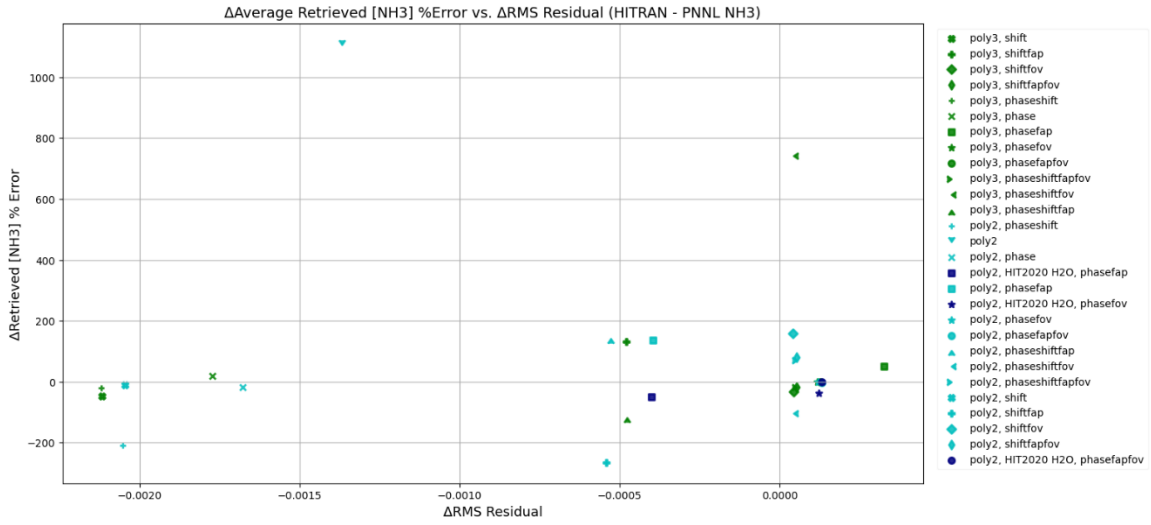

Figure 3-2: Difference in average retrieval percent error vs. difference in average RMS residual for retrieval configurations using HITRAN and PNNL spectroscopic databases (HITRAN value - PNNL value). Identical fitted parameter combinations are labelled with the same shapes, but green is used for fits with poly3 (quadratic transmission background) and cyan is used for fits with poly2 (linear transmission background). Navy is used for poly2 fits that additionally used a newer HITRAN database for H_2O lines (Updated HITRAN 2020 instead of 2004 in all other cases). PNNL out-performs HITRAN for points where ΔRMS > 0 & Δ%Error > 0.

Figure 3-3 focuses only on the HITRAN-driven retrievals from Figure 3-1. The FOV offset is included in the legend to help understand whether the algorithm is performing ‘mathematical gymnastics’ by fitting an unrealistic FOV starting from the initial (theoretical) value of 21.739 mrad.

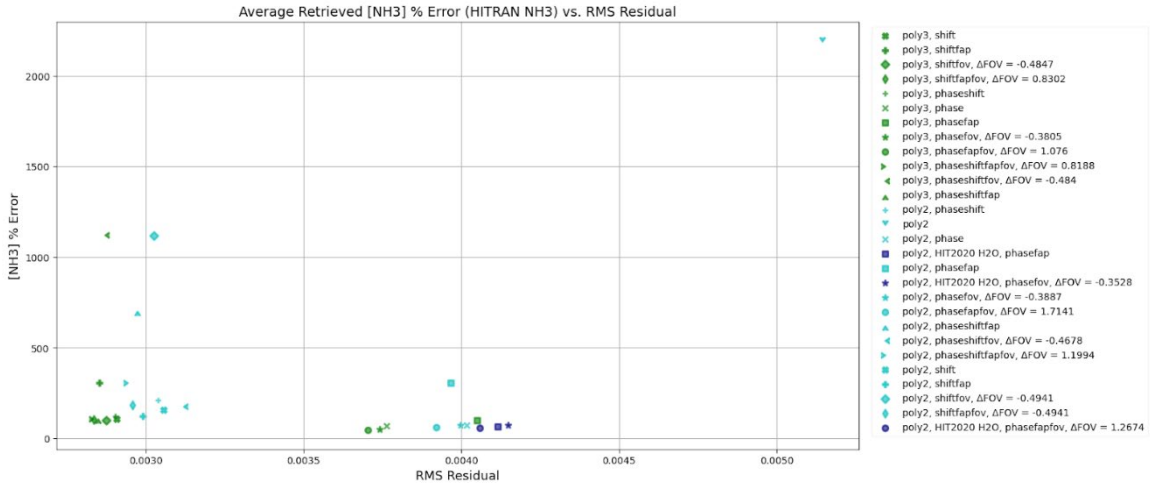

Figure 3-3: NH_3 retrieval percent error vs RMS residual for the HITRAN fits from Figure 3-1, with shape and color labelling the same as in Figure 3-2. The legend also indicates the fitted FOV offset from the initial value (theoretical = 21.739 mrad) for parameter combinations that fitted the FOV value.

The cluster of points around 0.0040 RMS all fitted ‘phase’, but not ‘shift’. The grouping around 0.0030 RMS all fitted ‘shift’ or ‘shift’ and ‘phase’. This leads to the conclusion that fitting ‘shift’ improved RMS by roughly 25% and that it is a critical parameter; given that practical FTIR spectrometers routinely lead to spectra with systematic shifts in the wavenumber axis, this makes sense. The PNNL version of Figure 3-3 is in Appendix A.3.1, Figure A-11, which also shows an improvement due to fitting shift *except* when only ‘shift’ and ‘poly3’ are fitted. Figure 3-4 shows the retrieved NH_3 concentration rather than the NLLS retrieved error as a function of RMS residual, only for HITRAN results. One can see that the ‘rough fit’ using only ‘poly2’ leads to an anomalously low NH_3 mixing ratio (~0.4 ppb) and the highest RMS residual. The other two clusters of results are formed from including or omitting the ‘shift’ parameter, as in Figure 3-3. NH_3 is found in the environment at ~1 ppb and we see that this can be considerably varied

between ~0.95 ppb and ~0.65 ppb through the choice of the remaining retrieval parameters. Notably, the use of 'poly3' to model a quadratic transmission background or 'poly2' to model a linear transmission background splits the retrieved NH_3 mixing ratios into two sub-clusters. Although the number of retrievals done with updated HITRAN 2020 water spectroscopy was limited (only 3 parameter combinations were completed), it was found that the maximum difference in the retrieved NH_3 concentration (due only to moving from HITRAN 2004 to updated HITRAN 2020 H_2O data) was less than ~0.1 ppb, or less than ~10% on the retrieved values of 1.2 – 1.4 ppb (see Figure 3-4). The retrievals using HITRAN 2020 water spectroscopy appear to be systematically different (they are offset by a similar amount in both RMS and NH_3 concentration) — see the upper middle section of Figure 3-4, comparing navy and cyan points. Note that these three retrievals did not fit the shift parameter.

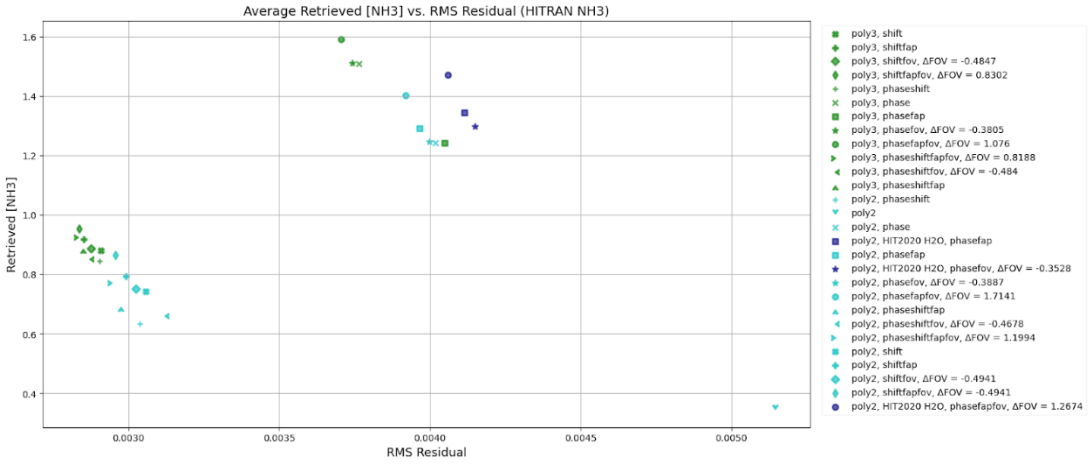

Figure 3-4: NH_3 concentration vs. RMS Residual. In colour (green indicates poly3, cyan indicates poly2, navy indicates poly2 and HITRAN 2020) and marker style (repeating for each colour) are the various parameter combinations fitted (see legend). The legend also includes the value of ΔFOV for combinations that fitted an FOV value.

Figure 3-4 was recreated for PNNL NH_3, but was placed in Appendix A.3.1, Figure A-12. Based on Figures 3-4 & A-12, the retrieved NH_3 concentration is quite sensitive to the fitting routine (ranging from approximately 0.4 – 1.6 ppb in a 24-hour average), and a group of points that fitted a 2nd degree polynomial (poly3) appear to be clustered around a minimum RMS value.

To compare PNNL and HITRAN NH_3 over the entire parameter space, they were plotted against each other in Figure 3-5 to check their correlation. The linear fit has a slope of ~0.9 and an offset of 0.1, suggesting that HITRAN retrieves higher concentrations in general, although there are many variables at play here. The methods produce similar results, in that the spread of retrieved NH_3 concentrations due to retrieval parameter choices is similar when using each database. The 'Pearson r' correlation coefficient was found to be 0.79, and corresponds to what is typically referred to as a 'strong' (0.60 – 0.79) or 'very strong' (0.80 – 1.00) correlation.

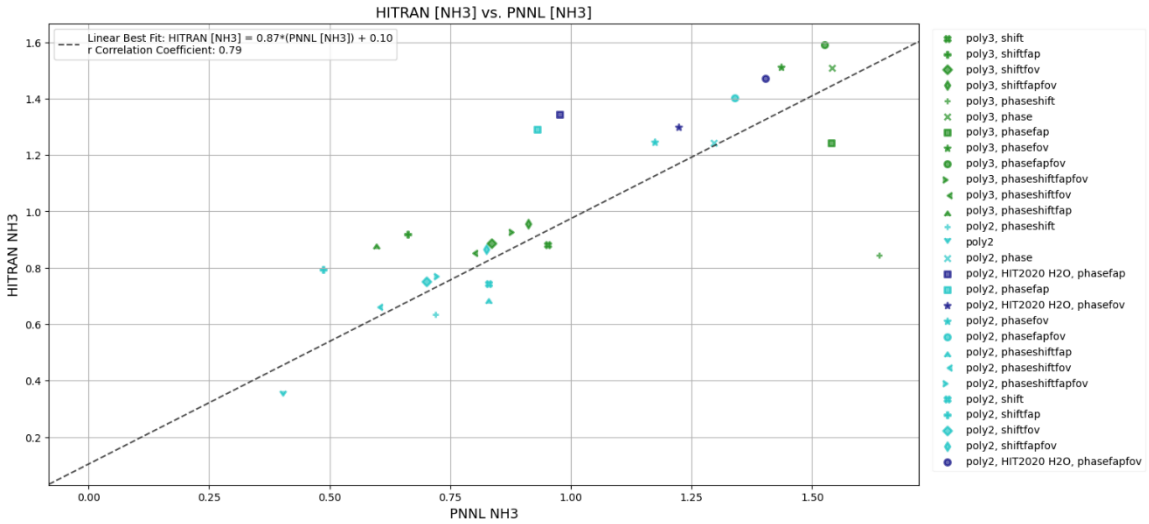

Figure 3-5: Concentration of NH_3, as retrieved using HITRAN NH_3 spectroscopic data for each parameter combination vs. that retrieved using a PNNL reference spectrum for NH_3. Parameter combinations are labelled and coloured as in Figure 3-2. A line of best fit is plotted as well, fitted with an offset.

3.1.2 – Carbon Monoxide (CO)

Using the same spectral data as the NH_3 analysis, and following the same procedure, the retrieval parameter sensitivity study was repeated for CO. NH_3 is a weakly absorbing gas, meaning that it is more difficult for the fitting algorithm to distinguish from the spectral features of other interfering gases. This potentially makes it inferior for gaining insight on the effects of each parameter on the quality of the fit, and inspired a recreation of the analysis for a gas with stronger absorption. CO was a perfect candidate for this. This analysis was done using the HITRAN spectroscopic database only, as the investigation no longer focused on the difference between using HITRAN or PNNL — this was left for future work. Figure 3-6 is a recreation of Figure 3-2 but for CO. A clear linear correlation can be seen, meaning the MALT output percent error is a better reflection of the fit quality in a CO retrieval, as opposed to for NH_3 (Figure 3-3). Interestingly, but not surprisingly, updated HITRAN 2020 H_2O points are optimal.

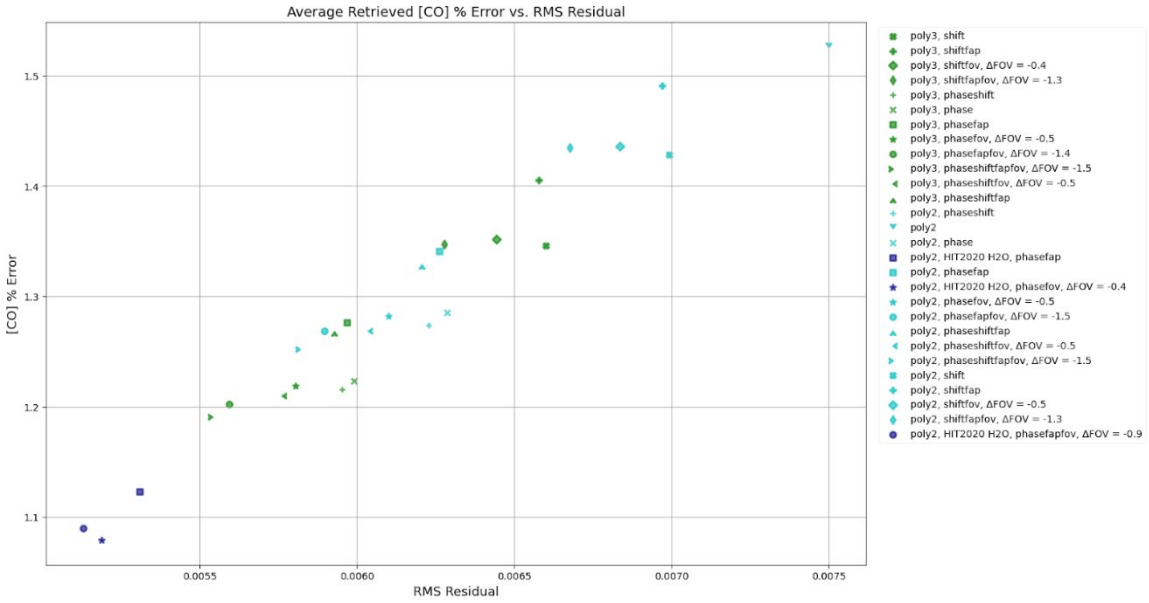

Figure 3-6: Retrieval Error vs RMS Residual for CO, with labels as in Figure 3-3 for NH_3.

Figure 3-7 also shows percent error vs RMS for CO, but only for retrievals that fitted FOV, allowing the fitted FOV to be used as a colour map. This investigates why fitting FOV does not always produce the same fitted FOV.

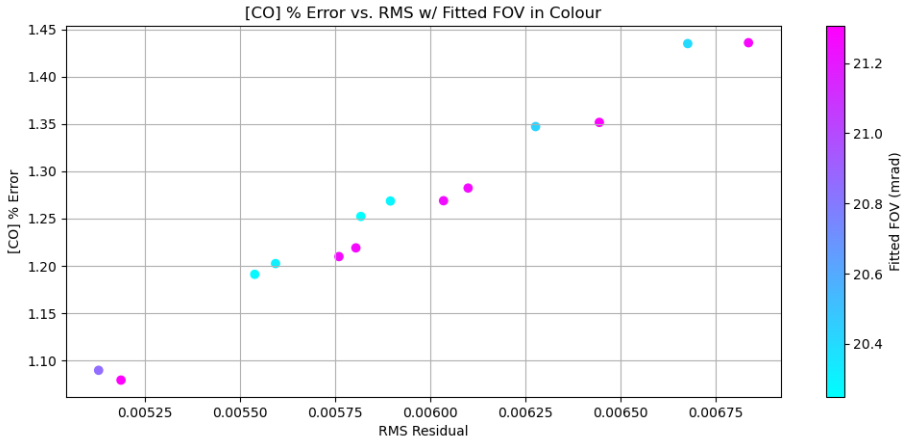

Figure 3-7: [CO] Retrieval Error vs RMS Residual, FOV fitted value in colour (21.739 mrad is the theoretical initial value).

Two solution clusters for FOV can be seen (magenta and cyan), although the % Error is not very sensitive (~1% changes vs ~4% changes). Cyan points (and the purple point) also fitted FAP, while magenta points did not fit FAP. This was determined using Figure 3-8, which labels the points in Figure 3-7 by the respective FOV-fitting parameter combinations used.

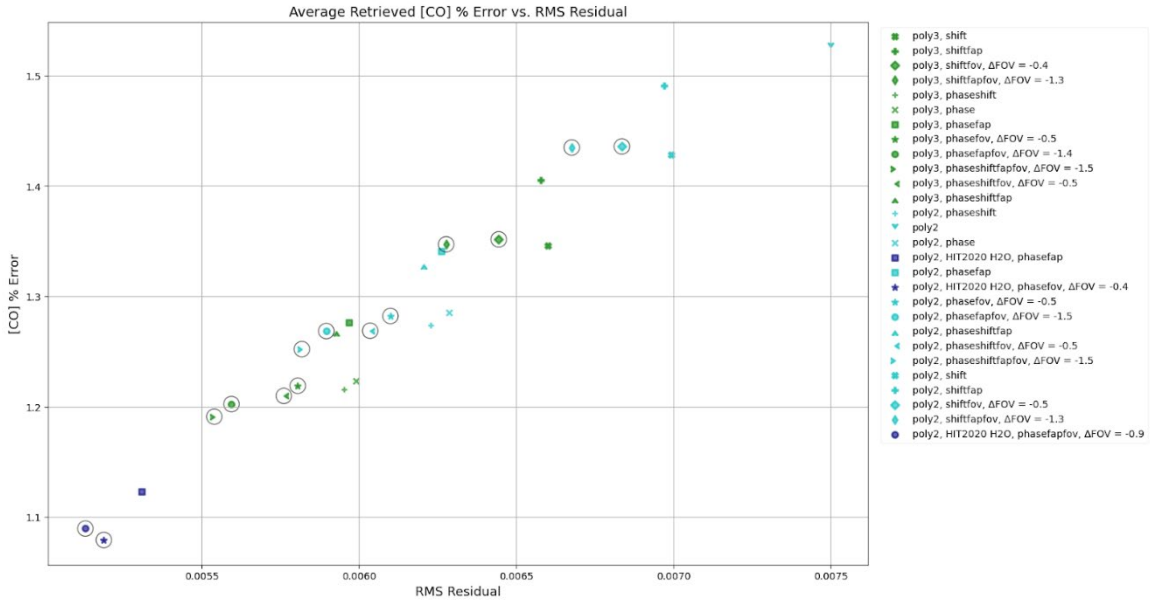

Figure 3-8: Same as Figure 3-6 but with FOV fits circled in black.

Figures 3-7 and 3-8 work together to show a small but systematic improvement in fit quality (reduced RMS residual and reduced percent error) when FAP is fitted together with FOV, except for the navy point with updated HITRAN 2020 H_2O spectroscopy (fitting them together reduced RMS residual but increased percent error). The fitted FOV value (without FAP fitting) decreases from 21.739 mrad (theoretical and initial fit value) to ~21.2 mrad (2.5% reduction); when FAP is also fitted the FOV fits to ~20.4 mrad (6.2% reduction from theoretical initial value), except when updated H_2O spectroscopy is used (~20.8 mrad or 4.3% reduction). Similar improvements in RMS are found for NH_3 when FAP is fitted alongside FOV, but they exist in the context of errors of ~100–1000% (Figure 3-3) and the retrieved FOV values increase by 5–10% from theoretical while FAP is being fit simultaneously (Figure A-7). It is apparent that the two line broadening

parameters are not completely independent of one another. This can also be seen in the average fit correlation matrices that are output by MALT, which are recorded in Appendix A.5 and show the correlations between each of the fitted parameters. That H_2O spectroscopy has an effect is not unexpected since many broad H_2O lines contaminate the CO retrieval window, with stronger absorption than in the NH_3 window. While more investigation of FOV, FAP, and the updated HITRAN 2020 H_2O linelist is needed, it makes sense that fitting vs not fitting FAP and FOV simultaneously leads to a different fitted FOV value since they are both broadening parameters and trade off one another.

Figure 3-9 continues the analysis by checking the sensitivity of the retrieved concentration of CO. Although it is not very sensitive to the parameter combination (~ ±1%), changing from fitting poly2 to poly3 for the continuum (i.e. from cyan to green in Figure 3-9) systematically translates CO values in the parameter space by a similar amount for all points (~5% reduction in RMS with ~0.5% increase in CO).

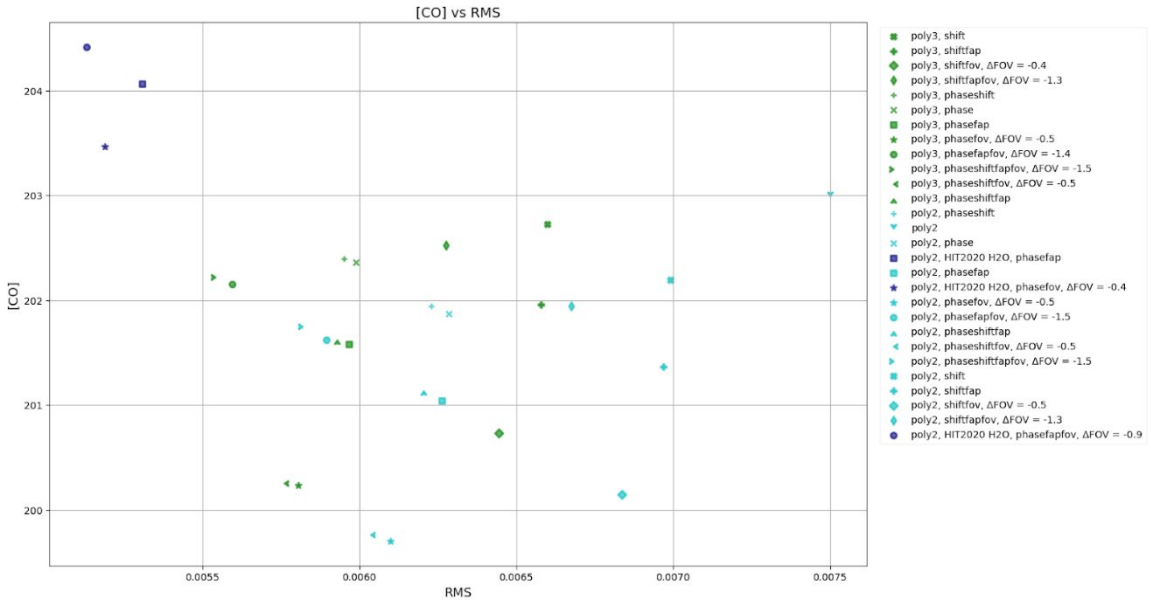

Figure 3-9: CO concentration vs RMS Residual, each point labelled by parameters fit.

More plots were made for NH_3, CO, and CO_2 (an interfering species in the CO retrieval window), in attempts to discover the intricacies of the relationships between these fit parameters and metrics (percent retrieval error, RMS residual), and they are included in Appendix A.3.1–A.3.3 to conserve space and focus the discussion.

3.2 – Detailed Investigation of the 'FOV' Spectral Fitting Parameter

In this section, the effect of the FOV parameter on a retrieval from a 1-month dataset is discussed. The effect of fitting or fixing the FOV parameter, with various initial values, is shown in Table 1 for NH_3 and in Table 2 for CO retrievals. The additional retrievals for NH_3, using CO FOV results, were done with an initial FOV of 20.189 mrad.

The pressure/temperature NaN data filter was not applied in this average FOV calculation since it had not been discovered yet (see Section 2.2), although the correctly filtered FOV from CO of ~20.2 mrad is close to and agrees with 20.189 mrad within uncertainty.

Table 1: Diagnostics from retrievals of NH_3 when fitting or fixing the FOV instrumental line shape (ILS) parameter. All retrievals were done on the same 1-month dataset between August and September 2021 (N = 9579 spectra for series 2 and 9575 for series 1, post-filtering).

	FOV fixed at theoretical value (21.739)	FOV fitted (NH_3)	FOV initialized using fitted FOV from CO retrievals (20.189), then fixed	FOV initialized using fitted FOV from CO retrievals (20.189), then fitted
Average [NH_3]	S1: 1.41 ppb S2: 1.49 ppb	S1: 1.37 ppb S2: 1.44 ppb	S1: 1.45 ppb S2: 1.53 ppb	S1: 1.38 ppb S2: 1.45 ppb
Average [NH_3] std deviation	S1: 0.56 S2: 0.50	S1: 0.56 S2: 0.51	S1: 0.56 S2: 0.51	S1: 0.58 S2: 0.53
Average %Error from MALT on [NH_3]	S1: 45.8 % S2: 18.6%	S1: 50.8% S2: 19.5%	S1: 34.2% S2: 18.4%	S1: 47.5% S2: 19.7%
Average RMS Residual	S1: 0.00325 S2: 0.00256	S1: 0.00324 S2: 0.00255	S1: 0.00327 S2: 0.00260	S1: 0.00329 S2: 0.00262
Average Retrieved FOV $\pm \sigma_{FOV}$	NA	S1: 22.8 ± 2.2 S2: 23.2 ± 1.9	NA	S1: 22.8 ± 2.3 S2: 23.1 ± 2.0
FOV Absolute Error from MALT (E_{FOV}) (average) $\pm \sigma_{E_{FOV}}$	NA	S1: 1.8 ± 22.1 S2: 1.0 ± 6.5	NA	S1: 2.7 ± 29.9 S2: 2.0 ± 24.3

Table 2: As for Table 1 but for CO retrievals from the same spectra.

	FOV fixed at 21.739 mrad (CO)	FOV fitted (CO)
Average [CO]	S1: 227.6 ppb S2: 218.7 ppb	S1: 228.5 ppb S2: 219.5 ppb
Average [CO] std deviation	S1: 124.1 S2: 103.1	S1: 125.5 S2: 104.4
Average % Error from MALT on [CO]	S1: 1.31% S2: 1.34%	S1: 1.24% S2: 1.26%
Average % Error from MALT on [CO_2]	S1: 2.56% S2: 2.58%	S1: 2.42% S2: 2.42%
Average RMS Residual	S1: 0.00626 S2: 0.00635	S1: 0.00589 S2: 0.00593
Average Retrieved FOV ± σ_{FOV}	NA	S1: 20.3 ± 0.3 S2: 20.2 ± 0.3
FOV Absolute Error from MALT (E_{FOV}) (average) ± $\sigma_{E_{FOV}}$	NA	S1: 0.3168 ± 0.3 S2: 0.32305 ± 0.3

As shown in Table 1, it was found that in both cases where FOV was fitted for NH_3, the average fitted FOV was approximately 22.8 mrad with a standard deviation of 2.19 mrad, agreeing with the theoretical value (21.739 mrad) within the NLLS algorithm uncertainty on FOV, although still ~1 mrad higher on average. Comparing the retrievals of NH_3 with and without fitting FOV, they are very similar (see Table 1 above), except that the percent error on NH_3 was significantly lower for the series 1 retrieval (45.8% → 34.2% — 45.8% is the second lowest series 1 percent error) when FOV was fixed to the value retrieved from the CO window and left fixed. Series 2 did not see the same large benefit from fixing FOV at the CO value (only 18.6% → 18.4%) but series 2 spectra are

less noisy to begin with because they used a retroreflector in better condition (note the lower RMS residuals for series 2, which are a partial reflection of spectral noise). This seems to imply that the FOV parameter becomes more impactful when dealing with noisier data. If that is the case, the initial FOV value is probably not the limiting problem in series 2 retrievals. Overall, the large improvement in NH_3 percent error when using the FOV from the CO window is sufficient to conclude that ~20.2 mrad is indeed optimal and should be implemented in future retrievals, but only with FOV then fixed at this value. Fitting FOV while starting from the CO-derived value (column 4 of Table 1) offers marginal (S1) to no (S2) benefits — this is because there is little FOV-related information in the broad NH_3 spectral features, and FOV fits to roughly the same value regardless of which initial value is used (see the second last row of Table 1). Regarding CO, fitting FOV yielded a slight improvement in the fit residual (RMS) and percent error (Table 2), also supporting this conclusion of an 'optimal' FOV value. There are two important limitations to these results. For NH_3 (Table 1), the spectral fitting region is suboptimal (Section 2.1). While the optimal NH_3 window also does not contain narrow CO lines that provide FOV information, the percent errors for NH_3 are likely to change in an optimal fitting window. As such, the numbers in Table 1 should not be over-interpreted. The second limitation that cautions against overinterpreting the numbers both in Table 1 and 2 is that FAP was fitted simultaneously to FOV for both NH_3 and CO. FOV and FAP are known to be correlated parameters that manifest similarly in the spectrum, and there are correlation matrices showing that in Appendix A.5. If Table 1 and

2 were repeated with FAP fitting turned off (i.e. fixed), we may expect the percent error on FOV to decrease (for sure), if not on CO or NH_3 concentrations as well (not for sure).

3.3 – Concentration Results and Application to Shipping Emissions Detection

In this section, retrieval results are summarized for species over one month's worth of series 2 spectral data (Table 3). Series 2 was chosen for time-series analysis that was not focused on ocean-air flux because the upper path retroreflector had higher reflectivity, and so the spectral data has a higher SNR. Based on the findings in section 3.2, the CO results correspond to those for series 2 with FOV fitted, which were identified as optimal (Table 2), while NH_3 results correspond to series 2 with FOV fixed at the CO-derived series 2 value.

Table 3: Average concentration, standard deviation, and retrieval diagnostics for trace gas retrievals over the Halifax harbour between 08/07/2021 – 09/10/2021, series 2 only (N = 9579).

Gas	Average Retrieved Concentration	σ_C	Average % Retrieval Error	Average RMS Residual
NH_3	1.5 ppb	0.5	18.4%	0.0026
HCOOH	1.7 ppb	0.4	20.8%	0.0034
CO	219.5 ppb	104.4	1.3%	0.0125
CO_2	444.2 ppm	18.1	2.4%	0.0125
OCS	1.0 ppb	0.1	40.8%	0.0121
O_3	27.4 ppb	9.8	2.7%	0.0015

CH_3OH	2.3 ppb	1.3	49.7%	0.0015

The gases directly linked to ship plumes and emissions are methanol, carbon monoxide, carbon dioxide, ozone, and ammonia, which were plotted together (Figure 3-10) for the preliminary identification of correlated concentration changes indicating ship plume events, which are typically characterized by increased CO, CO_2, CH_3OH, and NH_3, as well as O_3 titration (decrease in concentration) during temporally extended emission events.

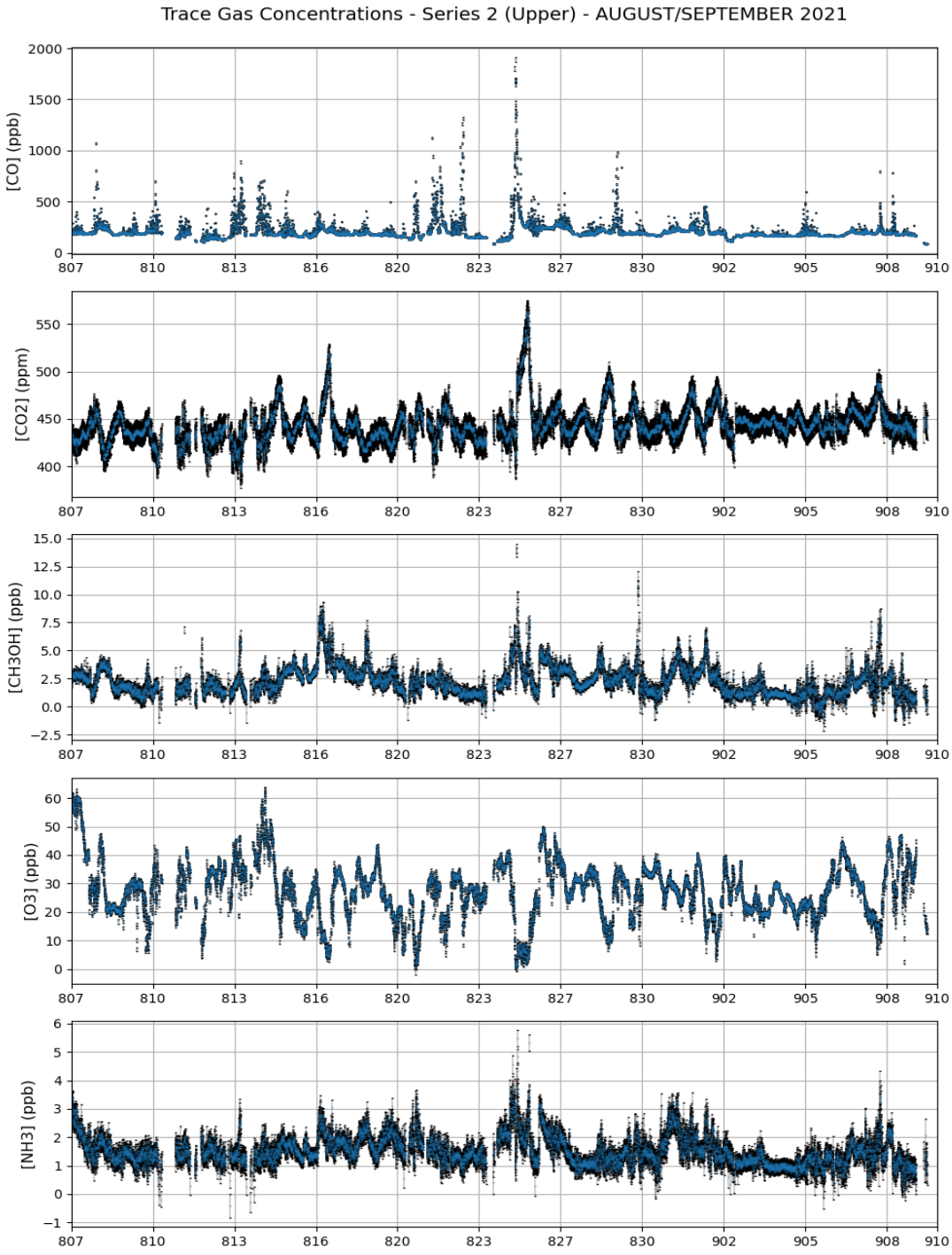

Figure 3-10: CO, CO_2, CH_3OH, O_3, and NH_3 concentrations (mixing ratios) from 08/07/2021 – 09/10/2021. Series 2 only; N = 9579 data points. Error bars represent the retrieval error from MALT (black) and the blue points show the retrieved concentration. The x-axis ticks show the date [MDD (month day)].

Many instances of elevated CO and CO_2 are visibly correlated with elevated CH_3OH and NH_3, as well as O_3 titrations, as expected. The peak in pollutants on ~08/25/2021 is particularly striking and signifies an extended emissions accumulation event. Further analysis with AIS marine traffic data is needed to accurately characterize all emissions in future work, as well as checking the correlations between each gas. We note that the methanol and ozone fitting (from a common spectral window) was done while also fitting the field of view, and in light of the results in tables 1 & 2, these concentration retrievals may be repeated without FOV fitting in the absence of time constraints, since in the case of NH_3 fitting FOV vs. fixing the FOV at the CO-derived value introduced a 6% positive bias in the mean results. However, OP-FTIR is generally considered very precise (e.g. Smith et al., 2011) and can capture temporal variations accurately; it is mainly the *variations* of CH_3OH and O_3 that were of importance for this preliminary result, rather than absolute concentrations.

3.4 – Concentration Results and Application to Air-Sea Flux

In this section, the 1-month concentration time series are examined from both the upper and lower open paths across the Halifax harbour, together with the vertical concentration differences that are proportional to ocean-air flux.

3.4.1 – NH_3

In Figure 3-11, NH_3 exhibits signs of a diurnal cycle, with an average concentration over the time period of 1.53 ppb, and a maximum at ~5.5 ppb (this peak is linked to the strong pollution event shown in Figure 3-10).

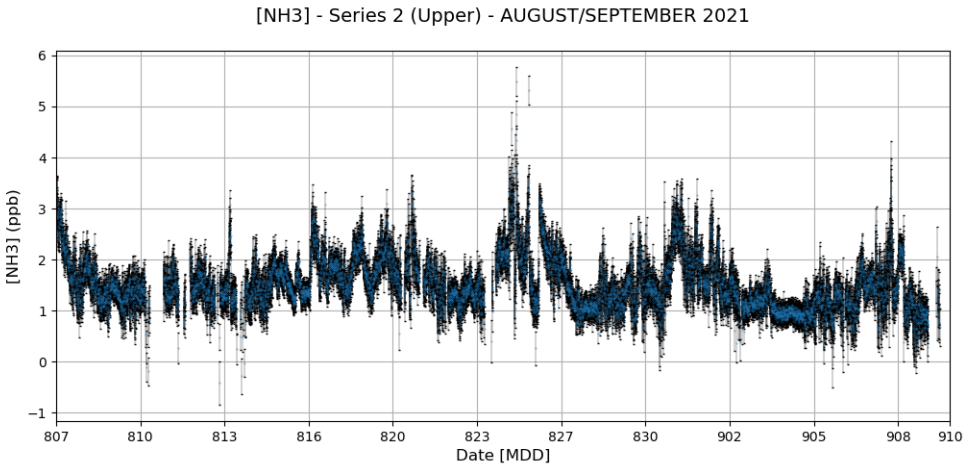

Figure 3-11: Concentration of NH_3 [ppb] over time, as in Figure 3-10.

Regarding air-sea flux, the vertical concentration difference for NH_3 over the entire time range appears to hover slightly above zero (Figure 3-12). Many of the data points have error bars which do not cross zero, meaning that the sign of the flux is more certain for these points. In this figure, the error bars represent the standard error of the binned data as described in section 2.4.

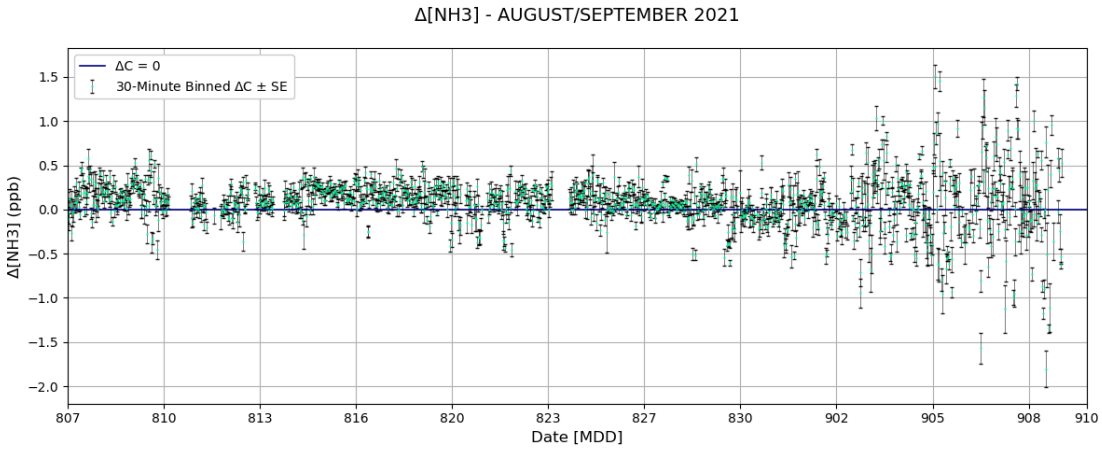

Figure 3-12: Concentration difference binned in 30-minute intervals (series 2 [upper] - series 1 [lower]) over time calculated from the retrieval of NH_3 for all data points after filtering (N = 9575). The error bars (standard error) are in black and the data points are in green. $\Delta C < 0$ indicates flux into ocean (sink) and $\Delta C < 0$ indicates flux out of the ocean (source).

Figure 3-12 suggests that the ocean is a net sink of ammonia in Halifax, NS, during this period of time. The data becomes noisy after ~09/02/2021, which is likely due to higher wind speeds (see Figure 2-1).

3.4.2 – CO_2

In addition to being useful in identifying ship plume signatures and the general need to track the atmospheric concentration of this important GHG, CO_2 also exhibits a significant positive concentration difference for the majority of the data, indicating an ocean sink (Figure 3-13). This agrees with the current understanding that the ocean is indeed a net sink for CO_2 near Nova Scotia and world-wide (e.g., NOAA PMEL Carbon Program, 2000).

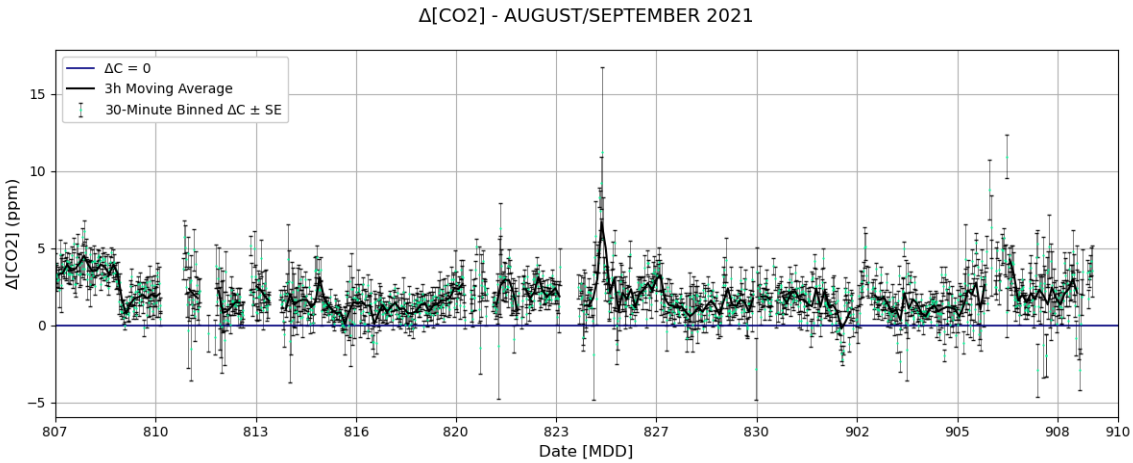

Figure 3-13: Same as Figure 3-12 but for $\Delta[CO_2]$, including a 3h moving average.

Regarding the general behaviour of this GHG, the diurnal cycle of CO_2 was examined for most days in the time series and was found to be heavily related to solar radiation intensity, as shown in Figure 3-14. This result is likely to be driven at least in part by plant respiration, because the CO_2 emitted from plant respiration is easily transported by wind and detected over the harbour. However, CO_2 is also emitted from port activities and all land-based fossil fuel burning, and so it does not always look like Figure 3-14. The accumulation and rapid fall of CO_2 on the morning of 8-17 is likely connected to suppressed nighttime mixing followed by sunrise and convection. Interestingly, Figure 3-15 shows a sawtooth-patterned variation in CO_2 during a period of rising concentration between roughly ‘81820’ and ‘81914’ (nearly 24 hours). Its cause is not clear, but it is shown in the next section to be linked to OCS variations.

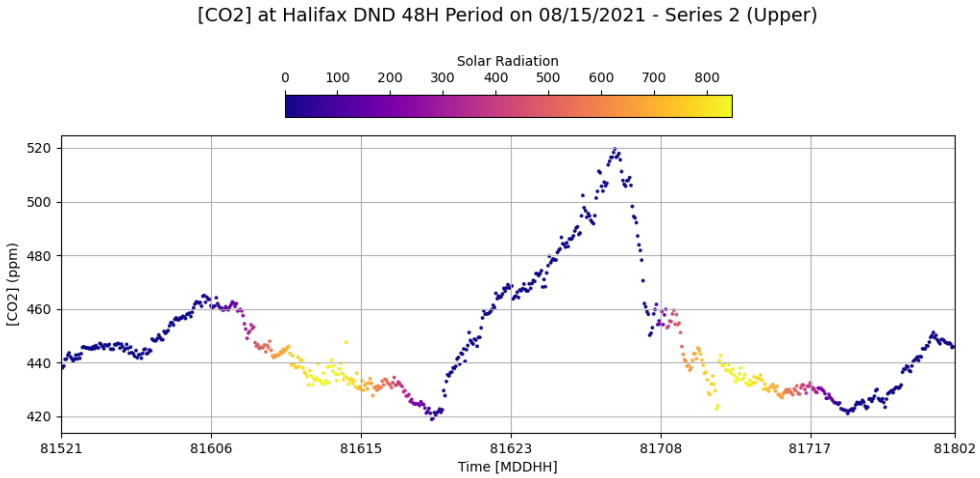

Figure 3-14: CO_2 concentration over a 48h time period between 08/15 and 08/18, 2021. Solar radiation intensity (W/m^2) is in colour.

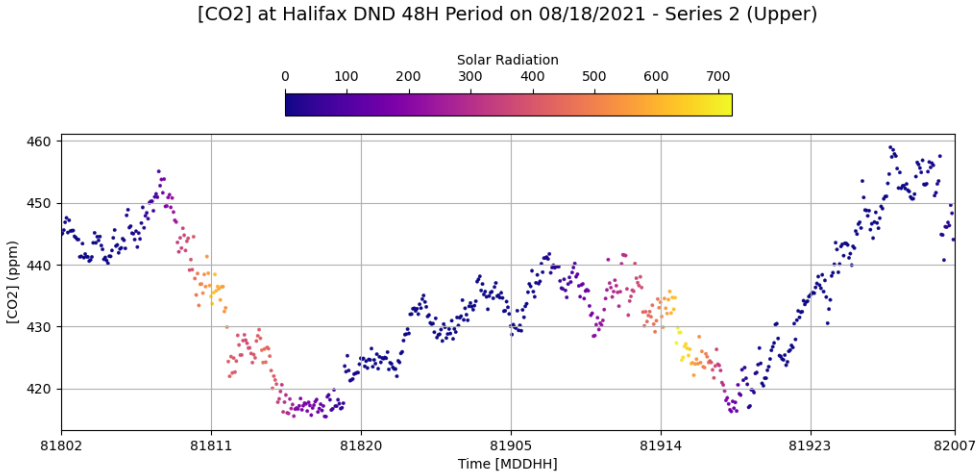

Figures 3-15: CO_2 concentration over a 48h time period between 08/18 and 08/20, 2021. Solar radiation intensity (W/m^2) is in colour.

3.4.3 – OCS

OCS is found in a spectral window partly overlapping with CO_2. Unlike CO_2, OCS is known to have an ocean source as opposed to an ocean sink. The diagnostic results from this OCS retrieval are shown in Table 3, and confirm that it is a low abundance gas that is retrieved with similar errors to NH_3. It shows less variability in

time than NH_3, which may be explained by a lack of strong anthropogenic sources for OCS. The time series of OCS concentration shows some diurnal variation (Figure 3-16).

Table 3-4: Diagnostics for the OCS retrieval. Fitted on 2021 data from 08/07 – 09/10. N = 9579 spectra for series 2 and 9575 for series 1.

	Poly3, phase, shift, fap fitted, FOV fixed at 20.2 mrad (based on CO – section 3.2)
Average [OCS]	S1: 1.08 ppb S2: 1.03 ppb
Average [OCS] std deviation	S1: 0.13 S2: 0.14
Average % Error from MALT on [OCS]	S1: 39.0% S2: 40.8%
Average RMS	S1: 0.0122 S2: 0.0121

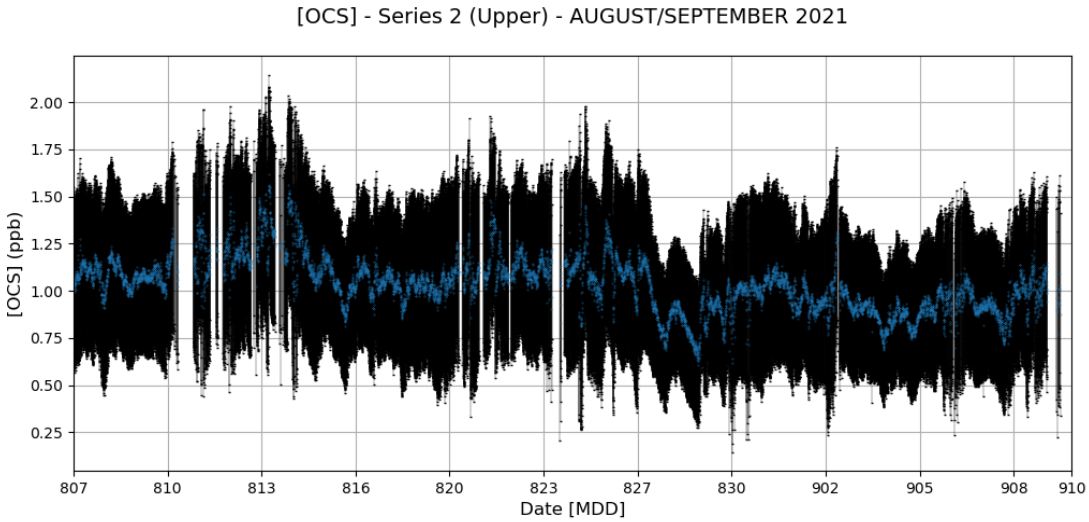

Figure 3-16: Concentration time series of OCS from 08/07 – 09/10, 2021. Error bars represent the MALT retrieval error.

This diurnal cycle appears somewhat related to solar intensity, and this permits a speculative explanation, i.e., production via photochemical formation — this hypothesis is supported by prior research, for example Ferek & Andreae (1984) document OCS production in the sea surface microlayer by ultraviolet radiation (rather than deeper in the ocean by microbes, like N_2O production). The 48h periods show some correlation with solar intensity, and after learning about an expected CO_2/OCS correlation (Commane et al., 2013), albeit in terrestrial environments, OCS was plotted alongside CO_2 over a 48h period (Figure 3-17). These temporally zoomed plots show a very strong anti-correlation with the CO_2 results, during both day and night on many days, and this correlation leads to a potential explanation for the variation pattern that was unexplained in the diurnal cycle of CO_2 (Figure 3-15) — Figure 3-15 is repeated within Figure 3-17 to show OCS at the same time.

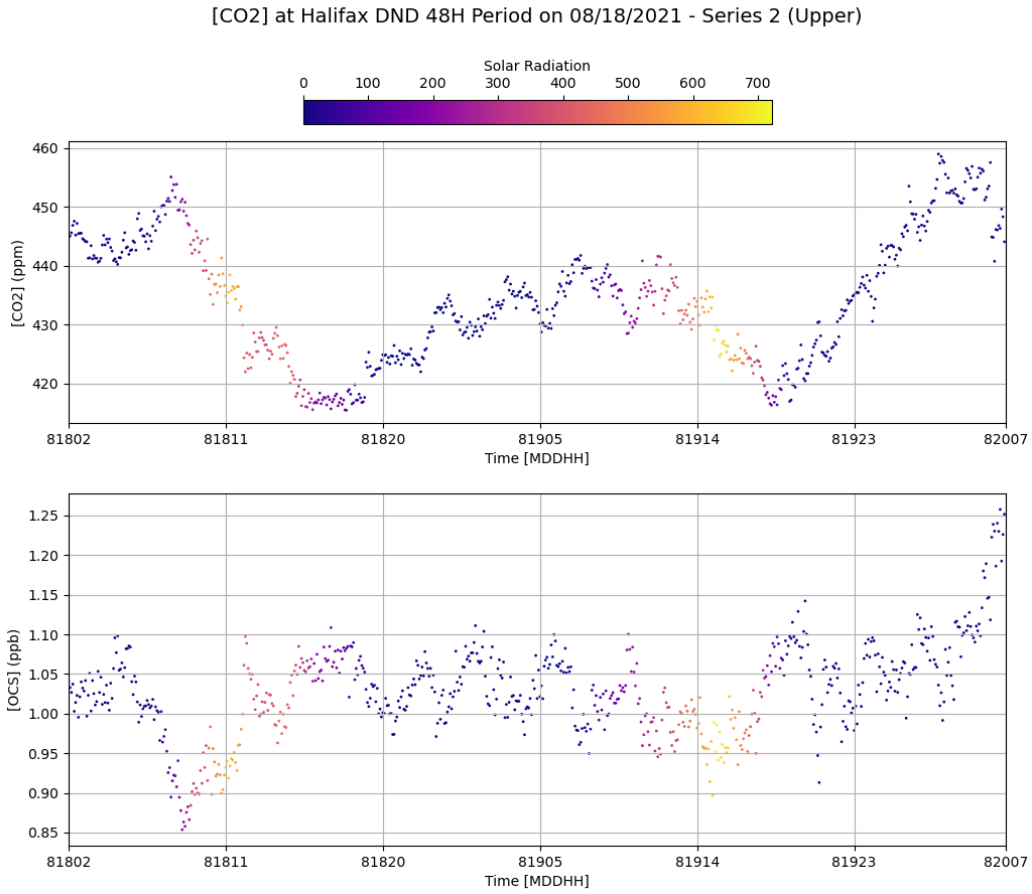

Figure 3-17: 48h time series of CO_2 (top panel) and OCS (bottom panel), colored by solar intensity.

The variations are seen to occur on a time scale of ~ 2 cycles/9h, or ~ 4.5h/cycle. This interesting variation does not occur as clearly every day (e.g. Figure 3-18, in which the saw-toothed pattern seen in Figure 3-17 is not seen as clearly, although the two molecules are still strongly anti-correlated).

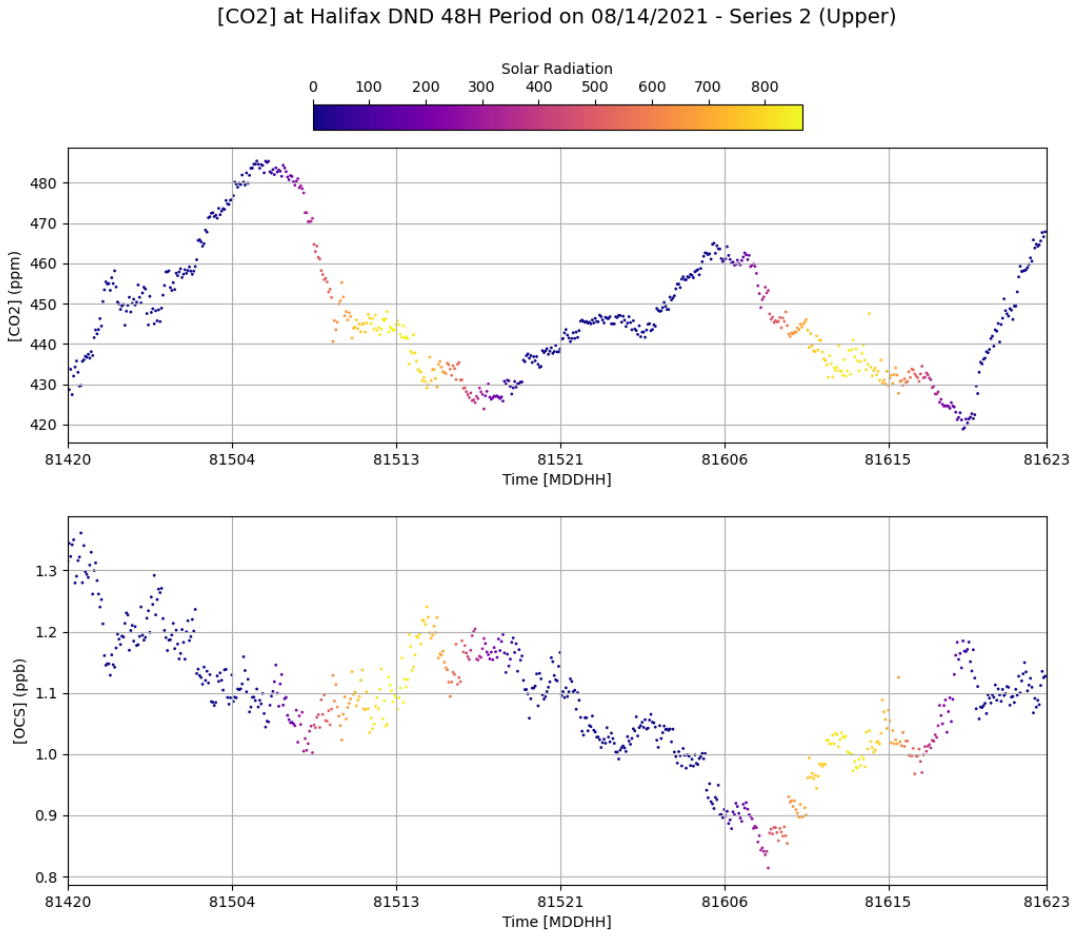

Figure 3-18: 48h time series of CO_2 (top) and OCS (bottom). Coloured by solar radiation in W/m^2.

For a general analysis of the CO_2-OCS correlation over the entire data set, they were plotted against each other and separated into a nighttime and daytime dataset, since it was not expected to be the same correlation (Figure 3-19) on account of the different physical processes taking place during day and night. This was done by using a solar intensity cut-off value of 100 W/m^2, simply based on the colour bar in Figure 3-18. A linear regression was fitted to the data using the scipy.stats.linregress module in Python. The value given for the y-intercept should be ignored, but was necessary to fit this negative slope. The fit

indicates that during the daytime, $\frac{\Delta OCS}{\Delta CO_2} \approx 0.0063$ ppb OCS increase / ppm CO_2 depletion. Note that here ΔOCS is generally positive and ΔCO_2 is generally negative, since during the daytime the observed trend is that *decreasing* levels of CO_2 accompany an increase in the concentration of OCS. During the nighttime, $\frac{\Delta OCS}{\Delta CO_2} \approx 0.0024$ ppb OCS depletion / ppm CO_2 increase. The data in Figure 3-19 was coloured by signal intensity (the data was already filtered as described in Section 2.2) to test whether it is the cause of the spread in the data, however that is not clearly the case. This is only an estimate since there is a significant degree of uncertainty here — the data is scattered with a relatively low correlation coefficient.

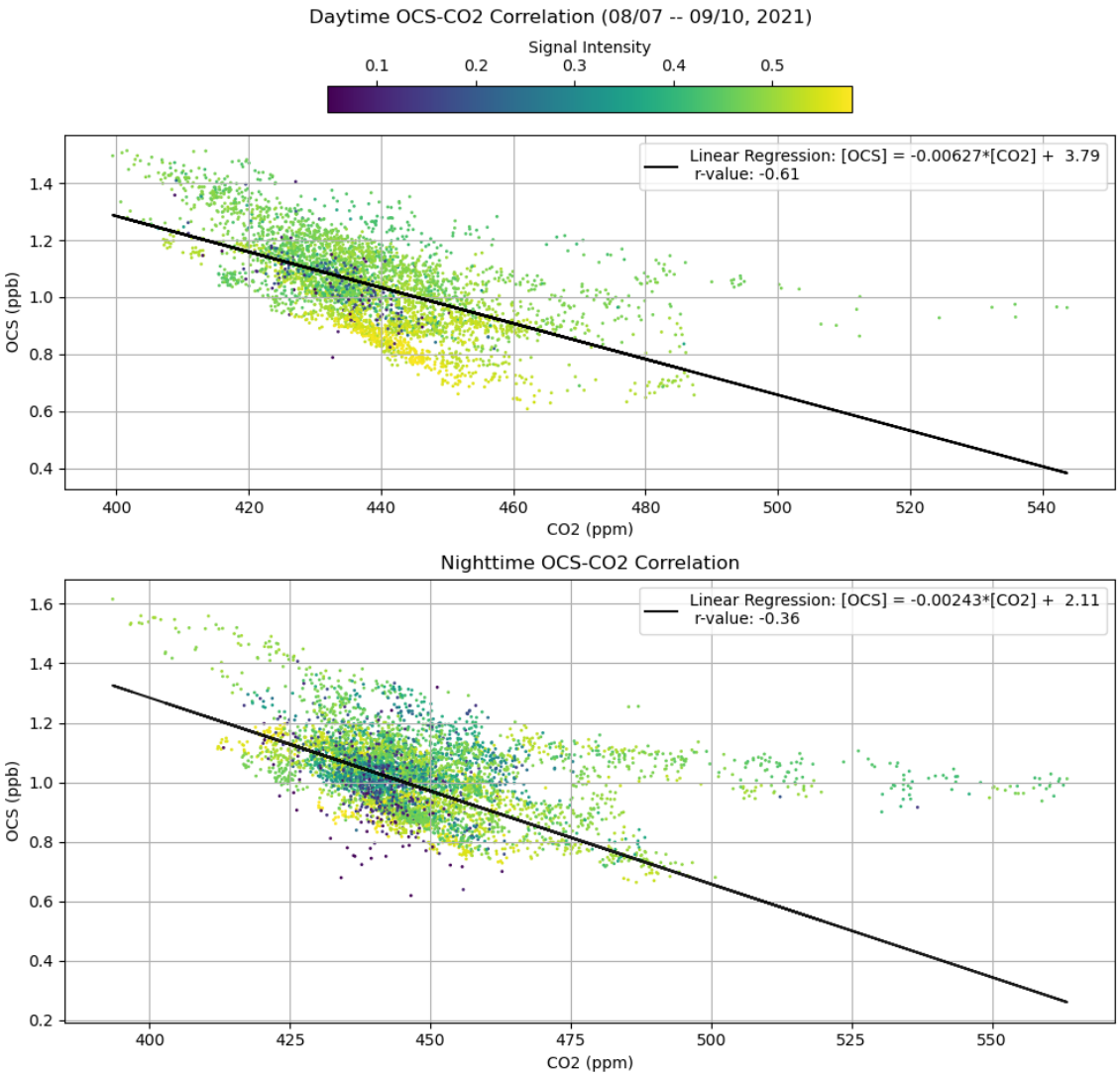

Figure 3-19: CO_2-OCS Correlation plot, for daytime correlation (top panel) and nighttime correlation (bottom panel). Points are coloured by signal intensity.

The observed correlation must be interpreted with some caution for two reasons. First, the OCS spectral feature lines up with a CO_2 branch, and retrieved concentrations show an average anti-correlation of -0.335 (Figure A-19), which is weak, but it may be statistically significant (significance was not tested). Second, the concentrations are changing due to several complex processes at the same time that are hard to disentangle

and require further study: air-sea gas exchange of CO_2 and OCS in opposite directions, terrestrial processes that affect CO_2 and OCS in different ways during day vs. night (with OCS processes much less understood), the production of OCS (and CO) within the sea surface microlayer being driven by UV as opposed to plant respiration being driven by blue and green light, and, *finally,* anthropogenic production of CO_2 in the atmosphere superimposed on both ocean and terrestrial biogenic processes – while modulated by dynamic effects on planetary boundary layer mixing.

Regarding OCS ocean-air flux, almost all concentration difference points lie below zero in Figure 3-20 and suggest a relatively constant ocean source of this trace gas between 08/07/2021 and 09/10/2021. A relatively larger concentration difference can be seen around 09/06/2021, but its cause remains unknown and it occurs during the noisier portion of the dataset.

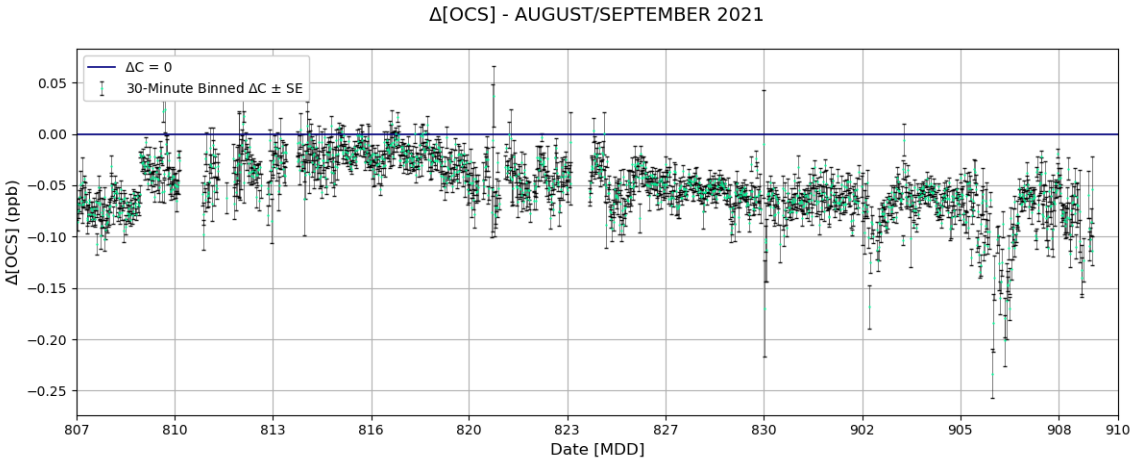

Figure 3-20: Same as Figure 3-12 but for Δ[OCS].

3.4.4 – HCOOH

HCOOH plays an important role in secondary organic aerosol formation, and thus cloud formation, an important factor in climate change modelling. This organic acid was retrieved over this dataset at an atmospheric mixing ratio of approximately 1.7 ppb. The results are summarized in Table 3-5, and its temporal variation can be seen in Figure 3-21.

Table 3-5: Diagnostics for the formic acid (HCOOH) retrieval ensemble. Fitted on 2021 data, 08/07 – 09/10. N = 9579 spectra for series 2 and 9575 for series 1. All values are post-filtering.

Average [HCOOH]	S1: 1.72 ppb S2: 1.65 ppb
Average [HCOOH] std deviation	S1: 0.49 S2: 0.39
Average % Error from MALT on [HCOOH]	S1: 28.7% S2: 20.8%
Average RMS	S1: 0.00351 S2: 0.00341

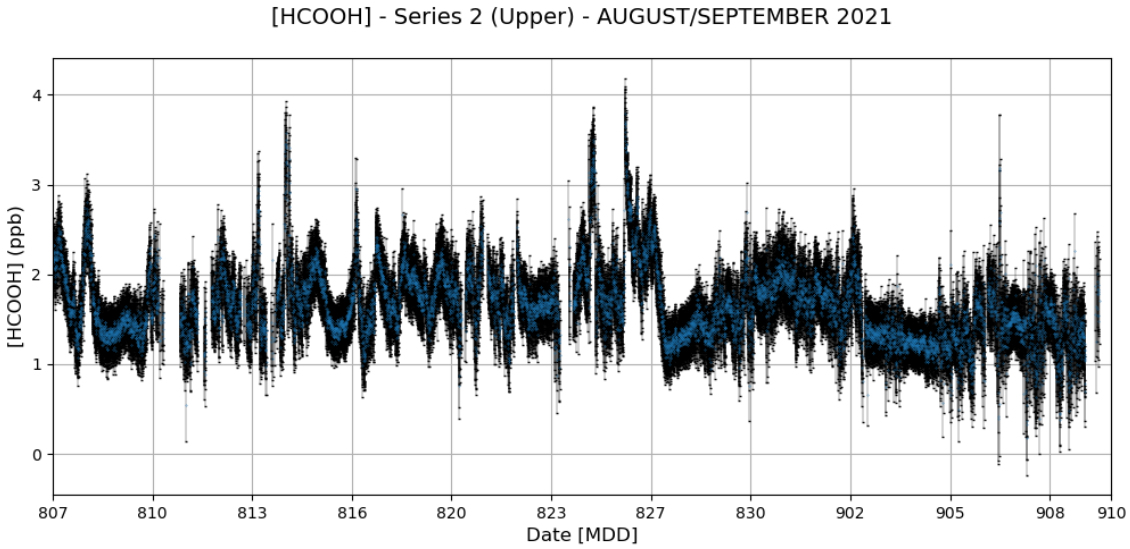

Figure 3-21: Concentration of HCOOH over time, as in Figure 3-10.

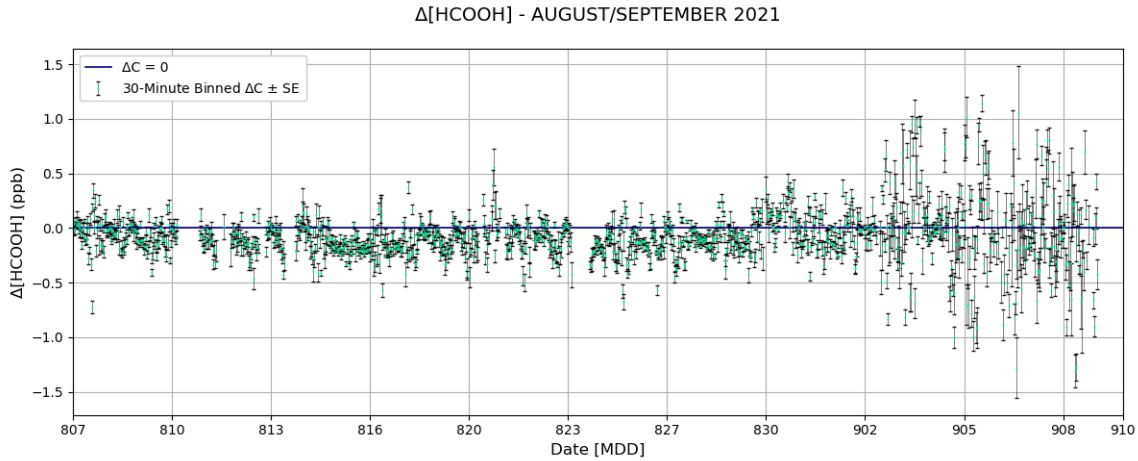

Figure 3-22: Δ[HCOOH] over time, as in Figure 3-12.

The majority of points in Figure 3-22 lie between 0 and -0.5, indicating an ocean source of HCOOH with a small standard error, and show some diurnal variations in the concentration difference itself. These variations on shorter timescales are easier to see on

a non-binned plot of the concentration difference with a 3-hour moving average plotted over top (Figure 3-23).

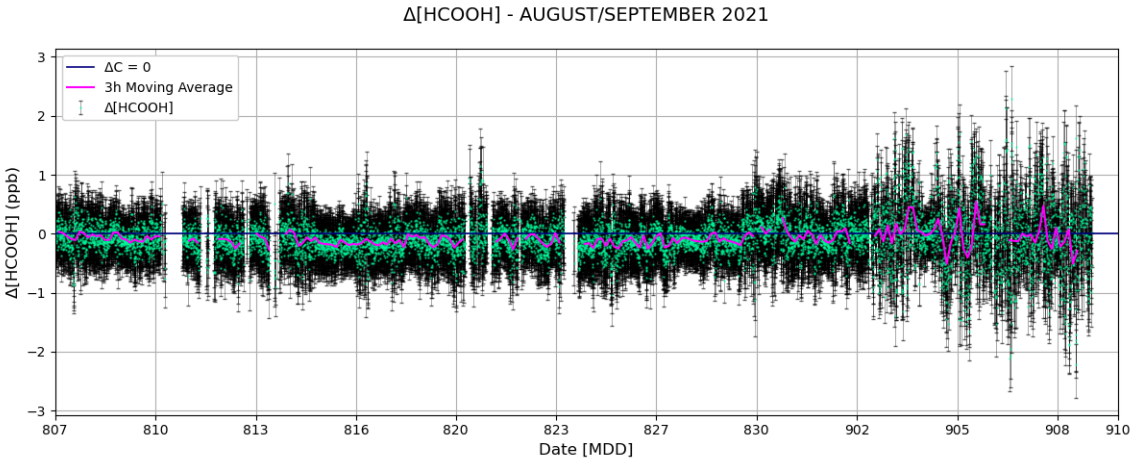

Figure 3-23: Δ[HCOOH] over time; the error bars are MALT errors.

Similar to the NH_3 results, the data becomes visibly noisier after 9/02. Finally, Figure 3-24 was made to analyze the behaviour of HCOOH concentration on a shorter time scale.

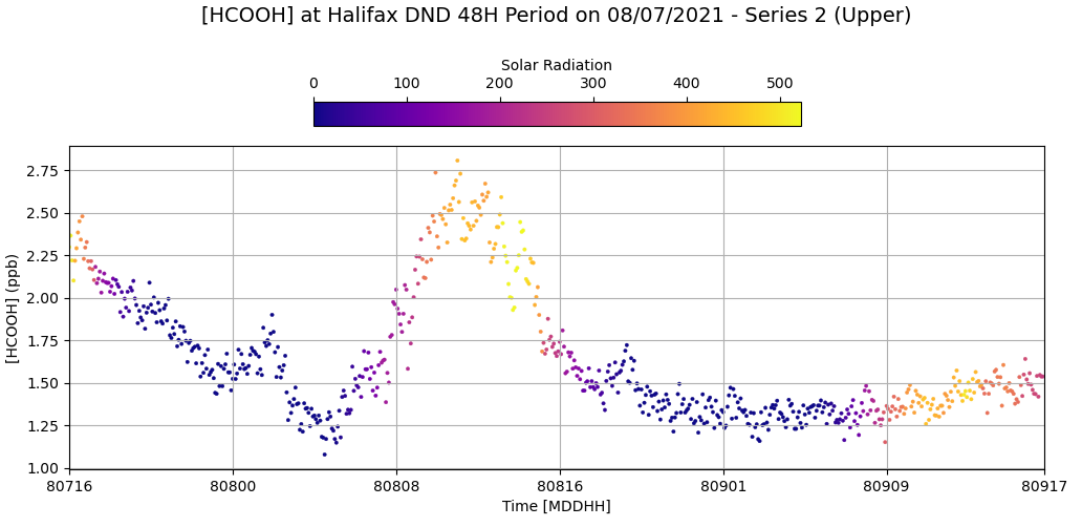

Figure 3-24: HCOOH concentration over 48h period with solar radiation in colour. The x-axis ticks represent the date and time (mddhh meaning the format is “month day day hour hour”).

Two peaks in Figure 3-24 (the first is cut off at the left side) are seen to correlate with solar intensity, however this is not always the case (e.g., right side). This could be a sign of a photochemical source of HCOOH.

3.4.5 – Note on O_3

A possible relationship between O_3 and UV intensity was observed (Figure 3-25), which would agree with expectations based on general textbook knowledge (e.g. Jacob, 1999) that O_3 is produced by photochemical reactions in the presence of UV light. This behaviour can be observed on multiple days, although O_3 is also influenced (destroyed) by the titrating effect of ship emissions of NO_X (= NO + NO_2) and atmospheric dynamics that play a role in concentrations over time. This peak in O_3 coincides with the central HCOOH peak in Figure 3-24.

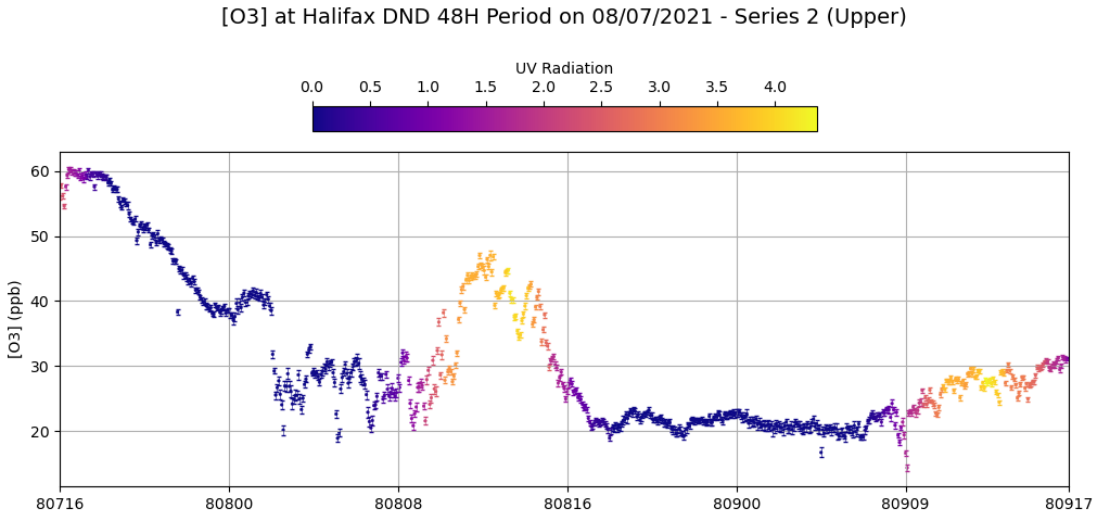

Figure 3-25: Same as Figure 3-24 but for ozone, with UV index in colour and MALT error as error bars.

4. Discussion

4.1 – Retrieval-Related Discussion (Results Sections 3.1 and 3.2)

In Section 3.1, the retrieval parameter choices were explored for NH_3 and CO, using as metrics of performance the NLLS retrieval error, the RMS residual of the fit, and the retrieved concentration, averaged over 24-hours of high-quality OP-FTIR spectra. These spectra were recorded in fair weather and at low relative humidity for Halifax, which maximizes IR signal intensity and minimizes spectral interference due to ubiquitous water vapour features. While the investigation was complex and many fitting parameter choices are possible, each affecting the ensemble mean metrics, some overall conclusions can be drawn from this sensitivity study. Small systematic effects were observed due to the chosen polynomial degree of the spectral continuum (poly2 → poly3 showed a clear linear translation in the CO percent error vs RMS plot (Figure 3-6)), as well as in the CO concentration vs RMS plot (Figure 3-9) with poly3 producing a slightly better fit as well as a slightly higher concentration of CO (Figure 3-9). There is also a systematic effect from fitting FAP and FOV simultaneously as opposed to individually in the CO retrievals (Figure 3-7 and Figure 3-8), however it remains unclear whether this is an improvement, or rather another example of overfitting due to the fact that these parameters trade off of each other — this is especially likely if the spectrum in question does not contain sufficient information (i.e. well-defined CO absorption lines) from which to fit a 'true' FOV value, which should be kept in mind. This FAP-FOV correlation can be seen in the correlation matrices in Appendix A.5 for retrievals that fitted both parameters simultaneously, which all show an average correlation of ~ –0.75

between FAP and FOV. The results from the parameter analysis in CO retrievals show that fitting FOV is also superior with this molecule itself as the target, which has the narrow spectral lines known to help with fitting FOV; moreover, the retrieved FOV offset from the initial theoretical value (between –1.5 and –0.4 in the legend of Figure 3-6) is much more stable from these optimal spectral lines than for NH_3 fits (between ~ –0.5 and +1.7 in the legend of Figure 3-3). The additional points with updated HITRAN 2020 water spectroscopy are not a complete sensitivity study, however they strongly suggest that using HITRAN 2020 water spectroscopy is optimal — this is not clearly shown in the NH_3 results, however NH_3 has weaker H_2O absorption in its window, and this could explain why the better fit performance of updated water spectroscopy is not as visible (the water lines in the CO window are also much larger and reach saturation (zero transmittance) (see Appendix A.1, Figure A-2) while those in the NH_3 window reach a minimum transmittance of ~0.5 (Figure 1-1). It could also be that there are other factors that are more significant than the H_2O spectroscopy limiting the quality of the NH_3 retrievals, since it is a very small absorption feature. Moving on to the other fitting parameters, the NH_3 analysis shows that fitting shift caused a ~25% reduction in the RMS value, meaning that it improved the quality of the retrieval. Similar to CO, the results from the NH_3 parameter analysis also show that fitting FOV is superior, however the FOV offset for the most optimal point is ~+0.9. This does not agree with the reduced FOV value from CO, which is in agreement with Smith et al. (2011), and points again to overfitting. It should be noted that optimal FOV is subject to change for every spectrometer.

Regarding the difference between PNNL and HITRAN, there were instances where PNNL performed better, although these were not for the most optimal fits (see Figure 3-2). In conclusion, there is not a radical difference between methods (at least for NH_3, in that window), although HITRAN is able to achieve slightly better results according to the metrics (see, e.g., figures 3-1, 3-2, and 3-5). This could change if dealing with a gas with stronger absorption features.

The results from section 3.2 indicate that the average FOV value from fitting CO (~20.2 mrad) leads to higher quality fits for low-abundance species like NH_3 where FOV fitting is uncertain, as compared to the theoretical manufacturer value (21.739 mrad). This is seen in a significant drop in the percent error on NH_3 (25% decrease) when fitted using this CO-derived FOV as a fixed input value for each fit (specifically in the series 1 result; thought to be due to higher noise levels due to lower signal intensity in the series 1 data set — it is possible that this parameter becomes more crucial when dealing with higher levels of noise in the spectrum). This reduced FOV value agrees with Smith et al. (2011), who also found a similarly lower-than-theoretical FOV value to be optimal, and leads to the conclusion that the most physically justified spectral fitting configuration for NH_3 is to fit 'phase', 'shift', and FAP (although FAP fitting still needs to be tested more rigorously to be certain), but to fix FOV to roughly 20.2 mrad. This FOV value of 20.2 mrad was derived from a CO retrieval that also fitted FAP, and since FAP and FOV are correlated parameters, it is hard to tell whether a CO retrieval that only fits FOV would yield a superior FOV value — this is being left for future research. In fact, fitting FOV is a poor decision in spectra where there is not enough information on line broadening, and

can lead to results with deceptively 'winning' diagnostics (i.e. low RMS, low percent error). This is seen in the results for CH_3OH (Appendix A.4, Table A-3), where the average fitted FOV value was ~25 mrad (unrealistically high), as well as in the parameter space plot for NH_3. Reassuringly, the concentrations of NH_3 and CO were not very sensitive to fitting/not fitting FOV (Tables 1 & 2) (although the FOV offset was not as large in these cases), so the results for CH_3OH concentration are likely not biased too strongly and remain useful for time-correlation analysis and detection of shipping plumes.

In summary of Section 3.1 and 3.2 results, the sensitivities of retrieved concentrations, fit residuals and retrieval errors are presented over the entire parameter space, however there are many variables at play and it remains difficult to identify a truly optimal set of fitted/fixed parameters without the presence of an objective truth. These results need to be interpreted on a case-by-case basis, and many additional plots containing interesting sensitivity-related findings are stored in Appendix A.3. For example, CO_2 concentration varies by ~10 ppm (~ 2%) due to changing from a linear to a quadratic transmission background polynomial, irrespective of the fitting configuration (Appendix A.3.3, Figure A-14). This sensitivity agrees with the findings of Smith et al. (2011) on the accuracy of OP-FTIR concentration retrievals of CO, CO_2 and CH_4 remaining "well below 10%" as compared to an actual 'truth' reference standard. It is fortunate that accuracy is less important than precision (here taken to mean measurement repeatability) when identifying trace gas correlations in the ambient atmosphere for ship plume identification (as was done in this work), as well as when analyzing vertical

concentration differences (which eliminate bias or accuracy errors) to determine air-sea flux values.

4.2 – Concentration and Concentration Difference Discussion (Results Sections 3.3 - 3.4)

A summary of the average vertical concentration difference results is presented in Table 4-1. To reiterate, the difference is defined as the upper path result minus the lower path result. The CO_2 and NH_3 results suggest a net ocean sink, while the OCS and HCOOH results indicate a net ocean source. CO_2, being a common interfering gas, was originally thought to be retrieved with highest quality from the same window as CO (2080 – 2133 cm^{-1}), however it was later discovered that the precision of the CO_2 result from the OCS window (2000 – 2100 cm^{-1}) was potentially superior (see Appendix A.6, Figure A-27 for a more in-depth discussion of this), likely because the CO_2 absorption feature in the OCS window contains more information (i.e., more absorption lines and a complete P-branch) (see Appendix A.1, Figure A-6). This other CO_2 result yields a notably different average concentration difference, so it is also recorded here in Table 4-1. For reference, the time series of the different CO_2 results from each of the spectral windows that fitted CO_2 as an interferer in this work (concentration and concentration difference) are recorded in Appendix A.6.

Table 4-1: Average concentration differences for CO_2, OCS, NH_3, and HCOOH. N = 9575 spectra. Positive numbers imply an ocean sink.

Gas	Mean Concentration Difference
$\Delta[CO_2]$ (from CO window)	1.885 ppm ± 2.637 ppm
$\Delta[CO_2]$ (from OCS window)	0.883 ppm ± 1.646 ppm
Δ[OCS]	-0.053 ppb ± 0.043 ppb
$\Delta[NH_3]$	0.082 ppb ± 0.378 ppb
Δ[HCOOH]	-0.073 ppb ± 0.337 ppb

5. Conclusions

Using 24 hours of high-quality OP-FTIR data (an ensemble of 360 spectra) to conduct an extensive analysis on which parameters should be fitted during spectral trace gas retrievals, it is concluded that fitting the 'FOV' parameter (related to line broadening) in a CO retrieval yields an optimal FOV value (~20.2 mrad for our spectrometer), and this parameter should likely be fixed at this value in all retrievals where the spectral information is insufficient to independently retrieve the FOV. It remains unclear whether a superior FOV value could be obtained by fitting CO without simultaneously fitting the 'FAP' parameter (a secondary parameter related to broadening), to avoid the correlation between the two parameters. Parameters 'phase' (manifesting as an asymmetry in all lineshapes), and 'shift' (horizontal wavenumber shift of each line) significantly affect the spectrum and should be fitted. An in-depth analysis of the FAP parameter remains to be done since it is not as intuitive, although it has been shown to help minimize fit RMS and

percent error when fitted (though this could be another case of overfitting). Finally, the degree of the continuum (i.e., transmission background) polynomial should be decided on a window-by-window basis. In this study, a quadratic (poly3) was found to be optimal in the spectral windows 2080 – 2133 cm^{-1} (CO and CO_2,) and 1078 – 1125 cm^{-1} (NH_3). The spectral database choice for trace gas line strength was investigated and it was found that using the updated HITRAN 2020 spectroscopic data for H_2O lines is optimal in these two wavenumber regions. Since HITRAN data is not available for all molecules, the PNNL database was also investigated, and results were compared for NH_3 because it is listed in both databases; retrieved NH_3 concentrations were highly correlated when using alternate databases.

The average concentrations of seven trace gases over 1 month of data (4-minute time resolution, N = 9575) were presented (Table 3-3), and Figure 3-10 shows the time series of shipping-related gases with various instances of ship emissions, characterized by increased levels of CO, CO_2, CH_3OH and NH_3, as well as O_3 titration during temporally extended pollution events. One especially large pollution accumulation event stands out in this time series on August 25th, 2021.

The vertical concentration differences for NH_3 and CO_2 indicate an ocean sink for these gases, while the results for HCOOH and OCS indicate an ocean source, in agreement with prior knowledge. For the first time ever, this work measured the concentration differences of these molecules at the air-sea interface using OP-FTIR, to be used in future ocean-air flux derivations with the flux-gradient approach. Whether a gas had an ocean source or sink was hypothesized based on whether the concentration

difference lay above or below zero. For example, the OCS concentration difference lies consistently below the zero line, indicating an ocean source (a negative concentration difference corresponds to a positive flux). These four gases exhibit diurnal variation; OCS and CO_2 show a strong cycle, with solar radiation influencing both of their diurnal cycles. HCOOH is also shown to be correlated with solar radiation on many occasions. O_3 appears to be correlated with UV intensity when not affected by ship emissions (although this was not extensively analyzed), as expected from general knowledge of O_3 photochemistry. The results are summarized in Table 3-3, and the calculated average concentration differences are summarized in Table 4-1.

Future Work

- Perform a more comprehensive analysis of shipping emissions using AIS data and gas correlations to determine the true extent of shipping emissions in Halifax (i.e. the emissions themselves and how they have changed over time since Wiacek et al. (2018)).
- Create diurnal variation plots to help explain gas behaviour.
- Do further work to understand the OCS-CO_2 relationship, including ocean processes, terrestrial emission processes, dynamical boundary layer effects, and atmospheric production of OCS from DMS.
- Calculate ocean-air fluxes for these gases (possible from Dec 2020 to Apr 2021, when 3-D sonic anemometer was measuring turbulence parameters).

Expand the analysis to other gases with a known air-sea flux. Compare calculated flux values to any reported literature values. A comparison of different time periods is also crucial to quantify how and whether the ocean-air fluxes of these gases are changing significantly over time.

- Better quantify the effect of using a reference spectrum for different gases. It is still unknown why PNNL out-performed HITRAN for certain parameter combinations in NH_3 retrievals, and whether that would remain true for a strongly absorbing gas like CO. HITRAN 2020 H_2O improvements in the CO retrieval warrant checking the effect of this new H_2O spectroscopy in all new gas retrievals.
- Investigate the behaviour of these trace gases in other seasons or years to study long term patterns and trends.
- Repeat the analysis of the FOV parameter in the retrievals of NH_3 and CO, but this time not fitting FAP in addition to FOV, in light of the result that FAP and FOV trade off of each other and systematically alter the fitted FOV in the CO spectral window (derived from Figure 3-8).
- Use simulated spectra to further analyze whether the instrumental parameters are fitting accurately.

Appendix

A.1 – Retrieval Window and Spectral Fit Examples

Listed here are example spectral fit plots for each of the targeted molecules, showing the recorded and simulated spectrum, the decomposition of the spectrum into the contributions from each trace gas present fitted in the spectral window, and the fit residual (as in Figure 1-1). When dealing with weakly-absorbing gases, a y-axis cut-off value was implemented to better show the absorption features in the middle panel.

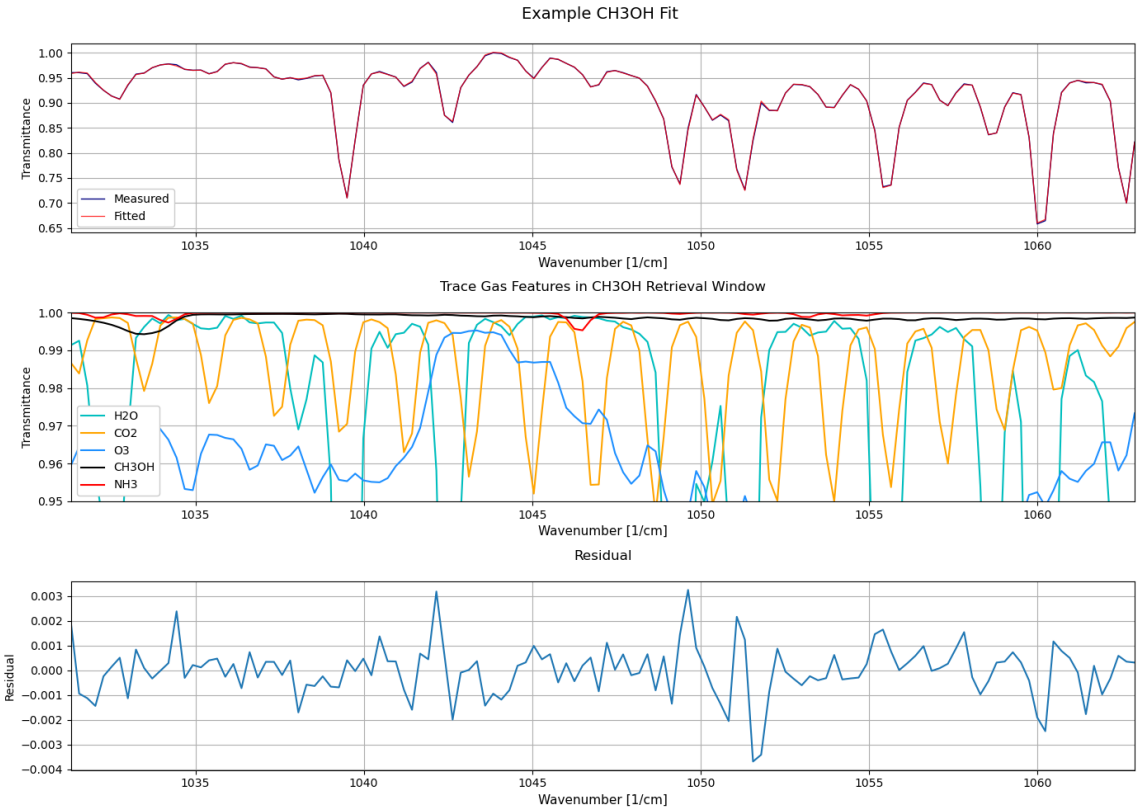

Figure A-1: CH_3OH fit, where O_3 is a jointly-fitted target gas, but NH_3 features are suboptimal. Top panel: Simulated and recorded spectrum. Middle panel: contributions from each trace gas with absorption features in the spectral window. Bottom panel: residual (recorded - simulated spectrum).

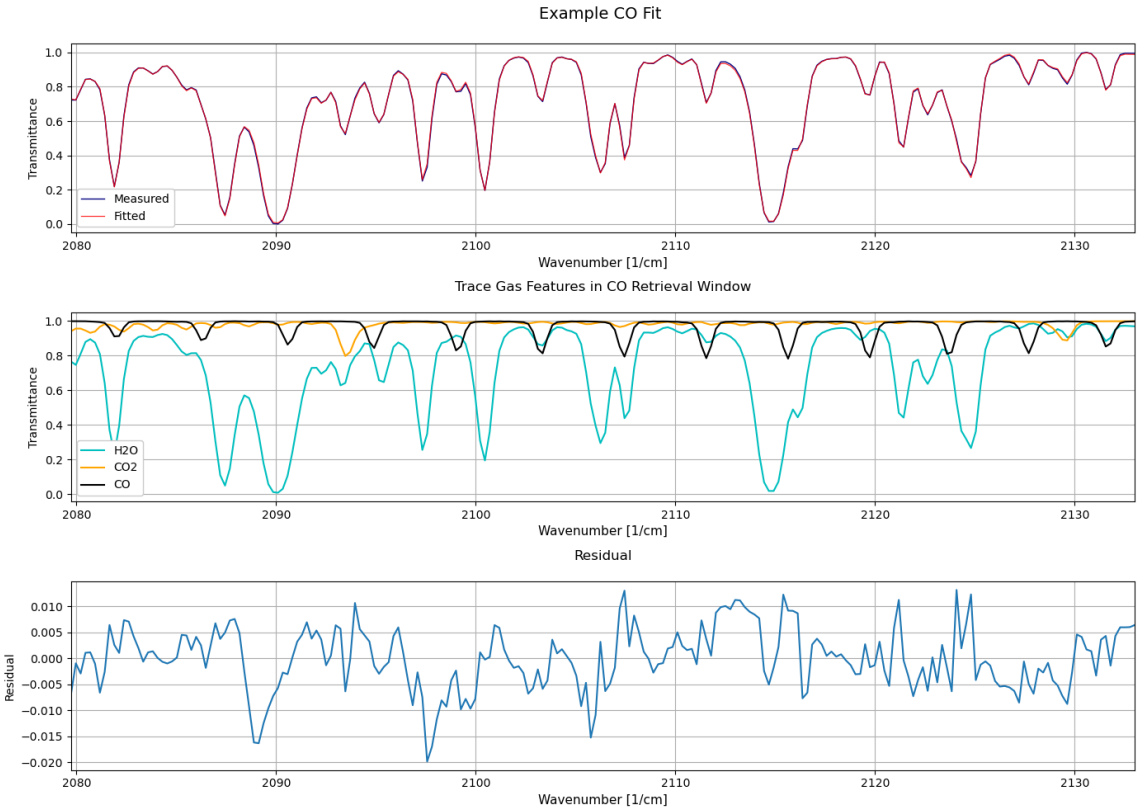

Figure A-2: As in Figure A-1 but for CO and CO_2 jointly retrieved as target gases.

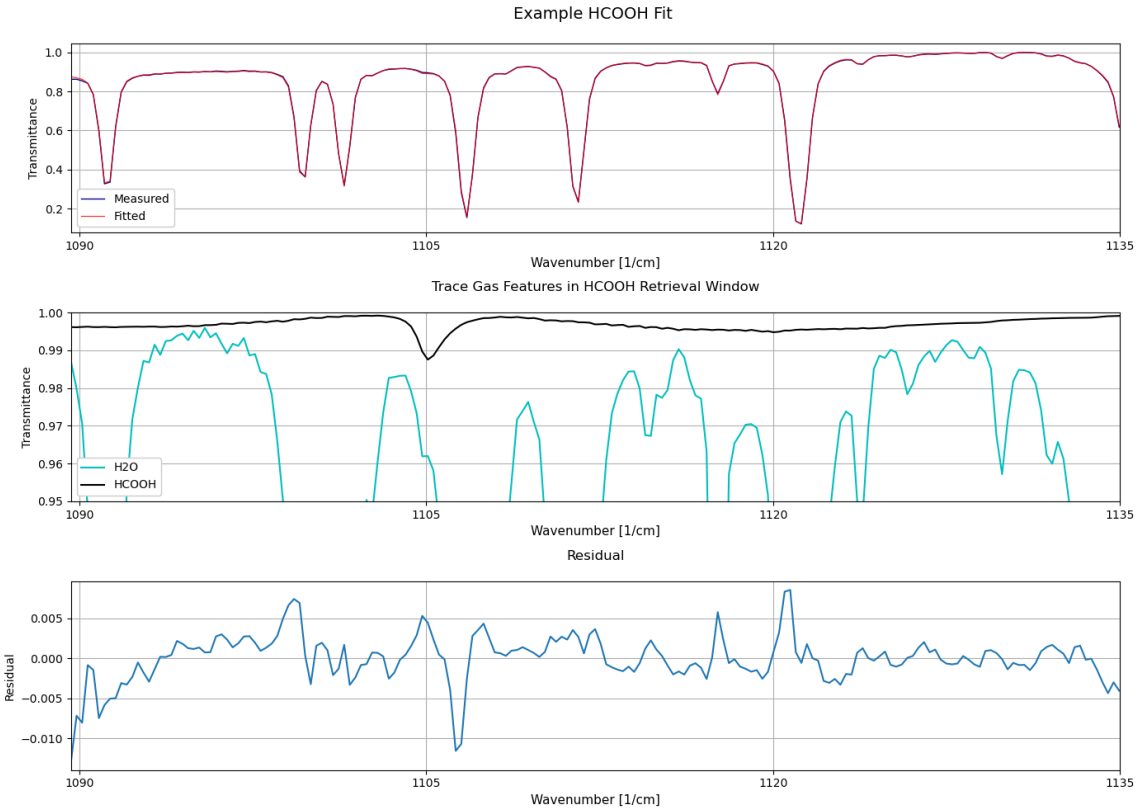

Figure A-3: As in Figure A-1 but for HCOOH.

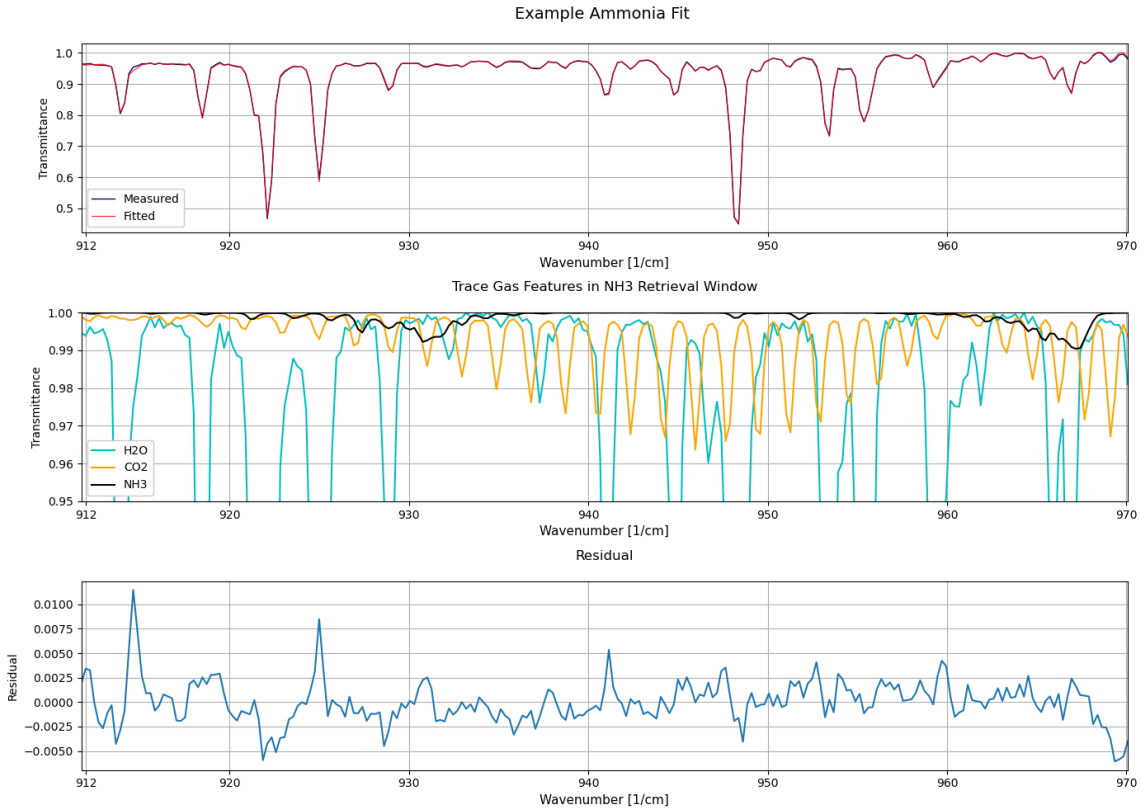

Figure A-4: As in Figure A-1 but for NH_3.

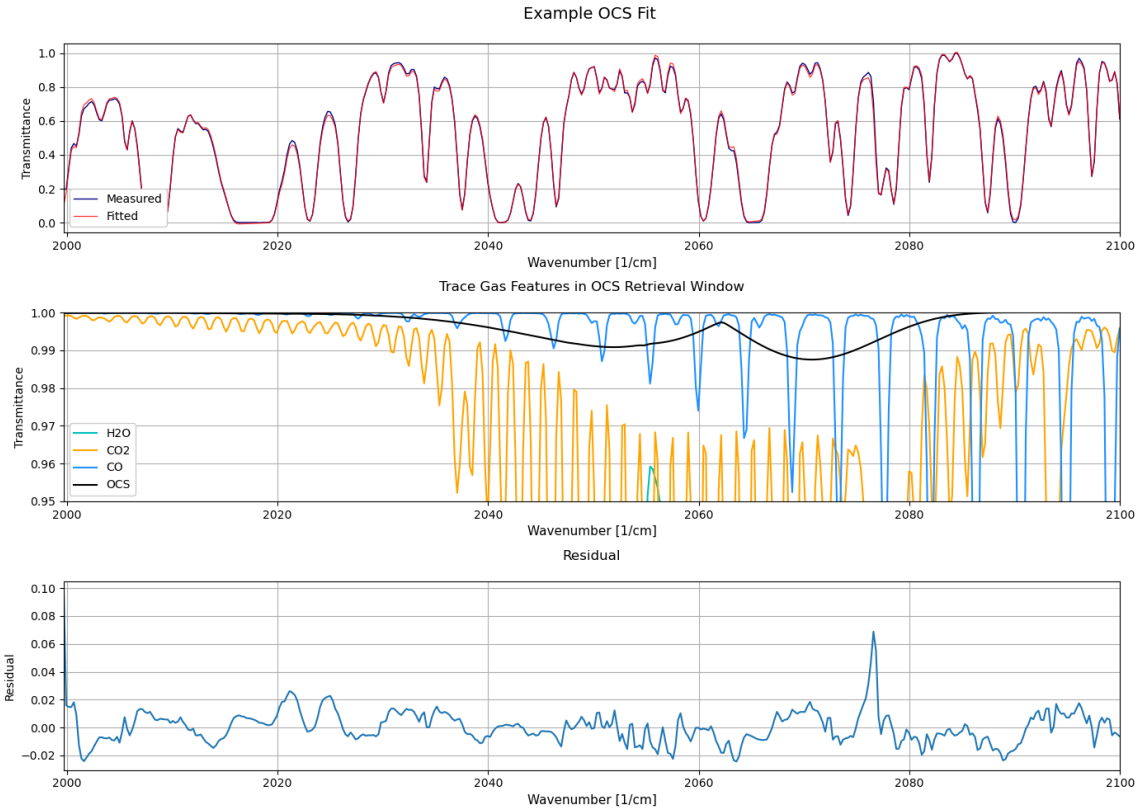

Figure A-5: As in Figure A-1 but for OCS. The CO_2 Q-branch 7% residual misfit near 2077 cm^{-1} is a known 'feature' of spectroscopic parameter deficiencies and it is de-weighted in MALT fits in this study.

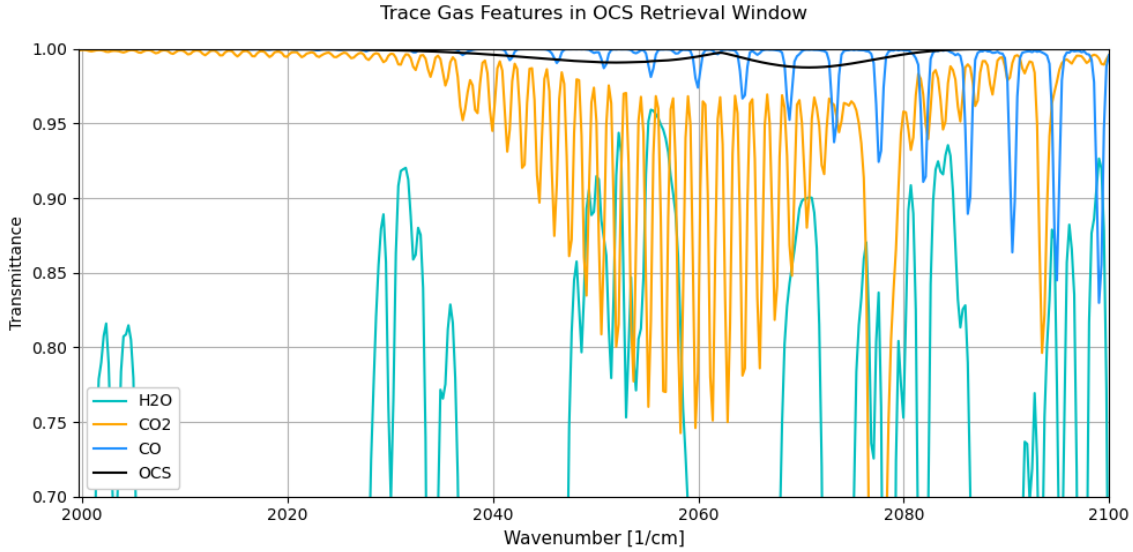

Figure A-6: The Middle panel of Figure A-5, but slightly zoomed out to better show the CO_2 feature in this window.

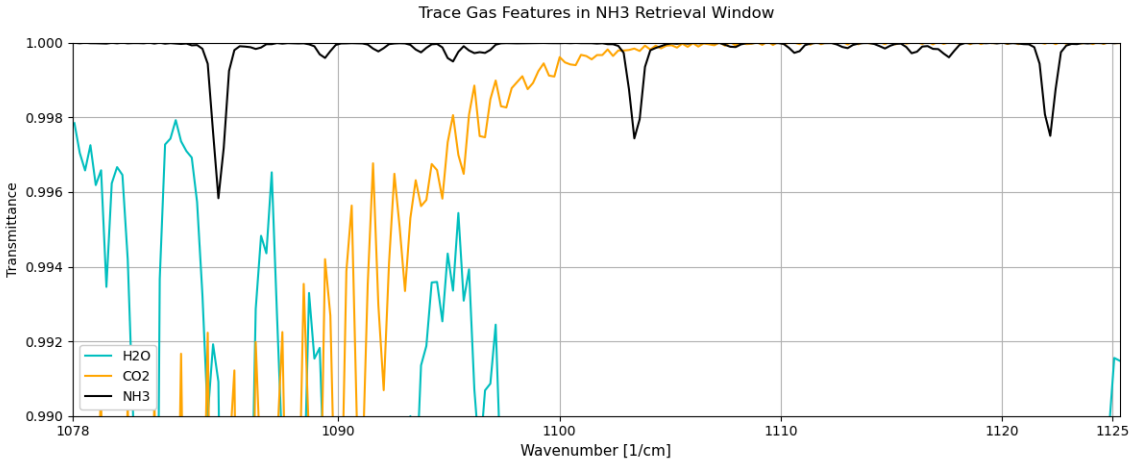

Figure A-7: Example fit 'component spectrum' for the spectral window used for the NH_3 parameter choices analysis.

A.2 – Retrieval Configuration Details

Table A-2: Fitting configuration used for each trace gas concentration retrieval. H_2O was always initialized at 1%, CO at 150 ppb, CO_2 at 400 ppm, and O_3 at 20 ppb, while CH_3OH, NH_3, HCOOH, and OCS were initialized at 1 ppb. HIT2020 indicates that the HITRAN 2020 database was used for the H_2O line list.

Gas	Fitted Parameters	Fixed Parameters	Spectral Window (cm^{-1})	Interfering Gases
CO/CO_2	poly3, phase, shift, fap, FOV	-	2080 – 2133	H_2O
CH_3OH/O_3	poly3, phase, shift fap, FOV	-	1031.5 – 1063	H_2O (HIT2020), CO_2, NH_3
NH_3	poly3 phase shift fap	FOV fixed at 20.2 mrad	912 – 970	H_2O, CO_2
OCS	poly3 phase shift fap	FOV fixed at 20.2 mrad	2000 – 2100	H_2O, CO, CO_2

HCOOH	poly2, phase, shift, fap	FOV fixed to 20.2 mrad	1090 – 1135	H_2O (HIT2020)

A.3 – Extra Figures from 3.1

This section shows plots from section 3.1 that were moved to the appendix to streamline the discussion of results, and they are separated into plots for NH_3, CO, and CO_2, analyzing the effects of spectral fitting parameter choices.

A.3.1 – NH_3 Parameter Space Plots

Figure A-8 was created to gain insight into how the retrieved concentration of NH_3 varies with respect to the fitted FOV value. It is however difficult to draw conclusions from, since there are many varying parameters. The same thing was done in Figure A-9, but for the percent error on NH_3 from MALT. Interestingly in Figure A-9, the points that fitted phase and FOV only (star-shaped points) cluster together just below a fitted FOV of 21.5 mrad. The addition of the FAP parameter increased the fitted FOV value, unlike for CO.

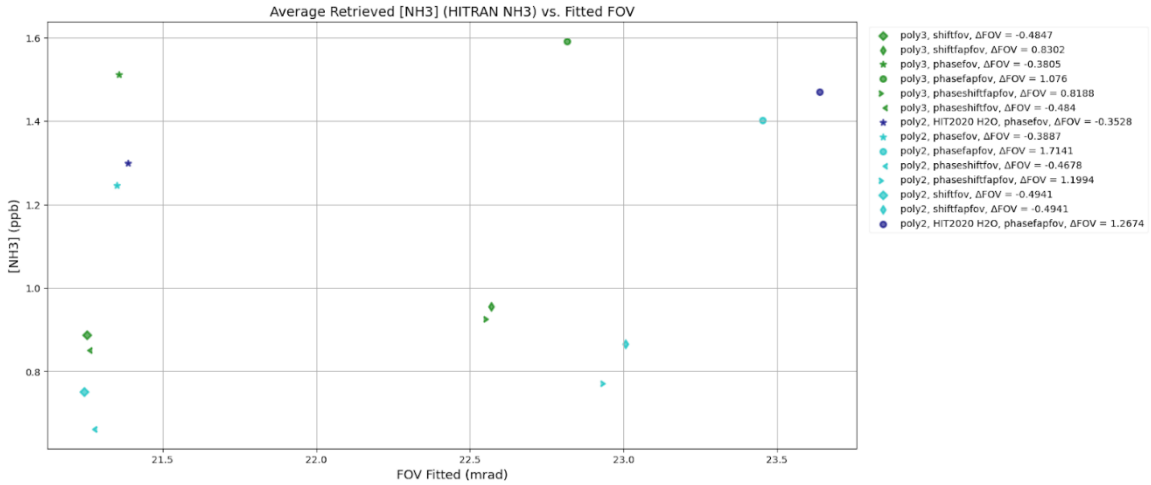

Figure A-8: NH_3 concentration vs. fitted FOV.

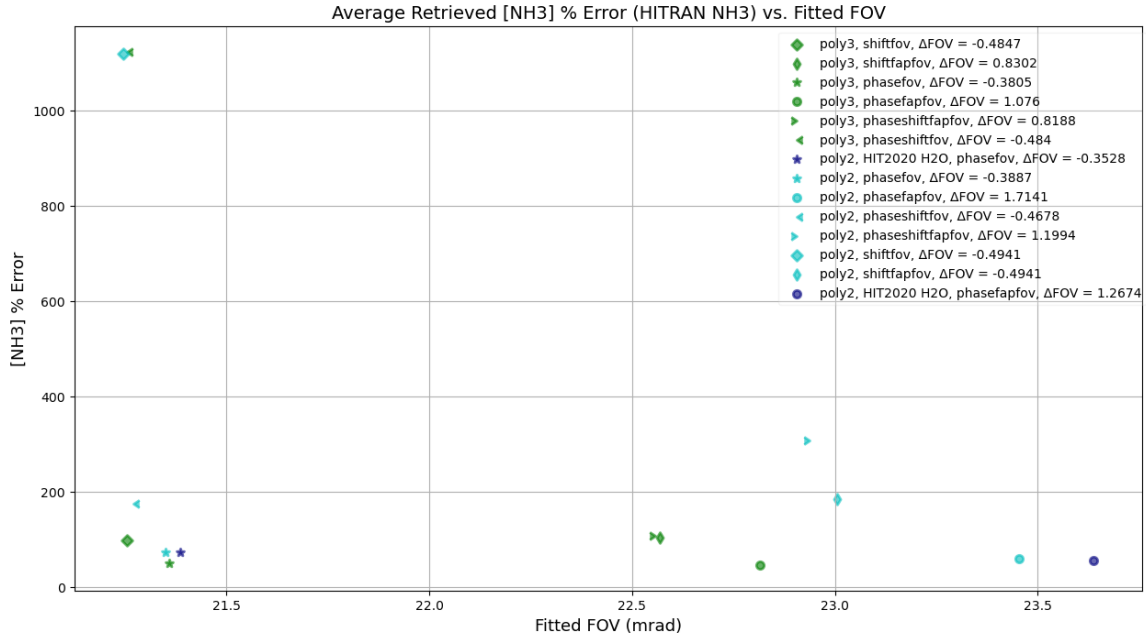

Figure A-9: NH_3 percent error vs. fitted FOV.

Also worthy of checking was whether overfitting was at play. This was checked via Figure A-10. Again it is difficult to identify the line between true optimization and overfitting. The points are coloured by the number of parameters fitted (including the continuum parameters poly1 (representing the 100% level of the continuum as a

horizontal line), poly2 and poly3). Within the cluster of fits that fitted the (necessary) shift parameter (cluster on the left, like in Figure 3-3) there is some evidence that more fit parameters minimize % Error and RMS, except for one pink point in the cluster with % Error > 1000.

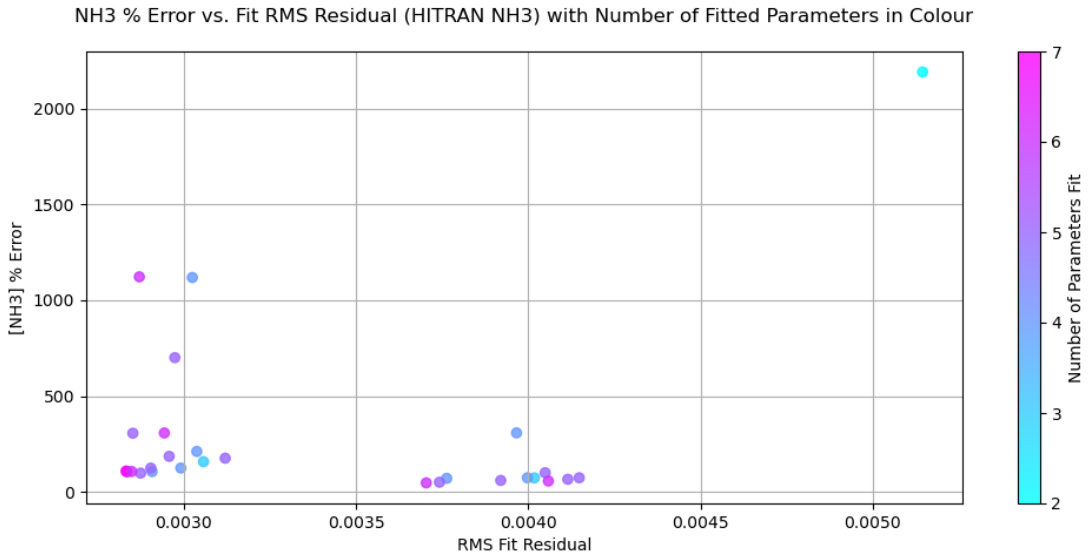

Figure A-10: NH_3 % error (as reported by MALT) plotted vs. RMS fit residual only for HITRAN NH_3.

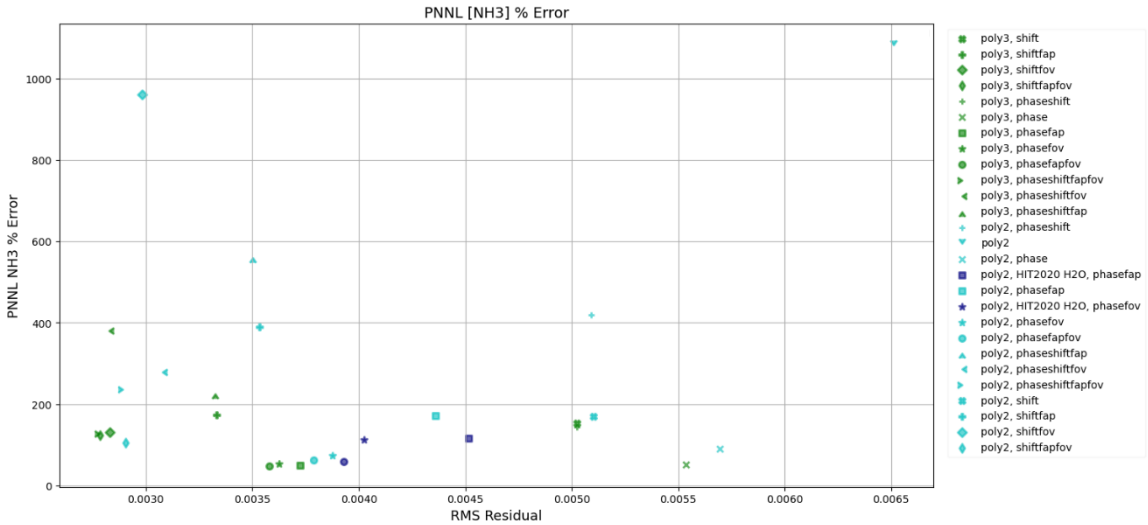

Figure A-11: Same as Figure 3-3 but for PNNL NH_3.

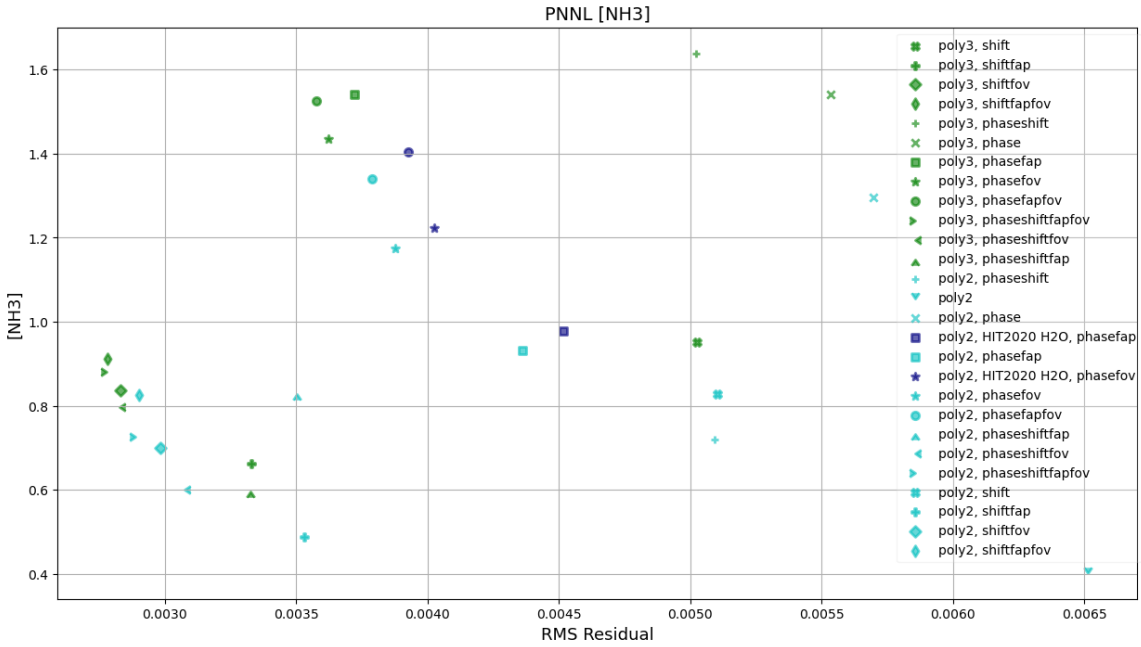

Figure A-12: Same as Figure 3-4, but for PNNL NH_3.

A.3.2 – CO Parameter Space Plots

Figure A-13 was made to investigate whether the MALT algorithm error is a reliable indicator of how well the fit is performing. Interestingly, the points are all equivalent within MALT error, and all error bars are similar in size.

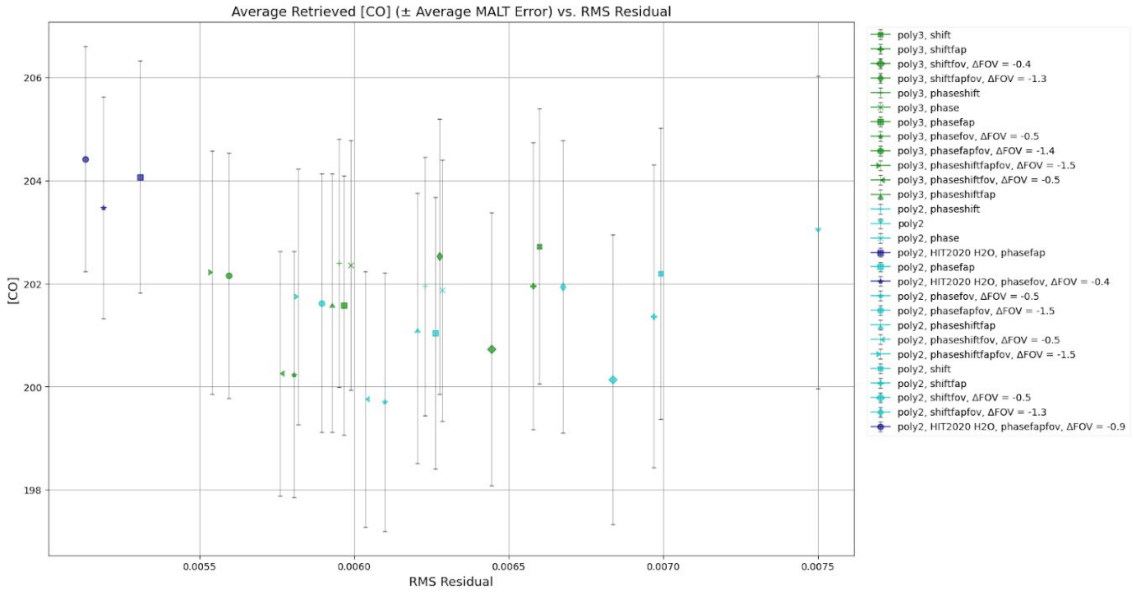

Figure A-13: CO concentration vs RMS Residual, with error bars from the MALT absolute error. Each point is labelled by parameters fit.

A.3.3 – CO_2 Parameter Space Plots

Figure A-14 shows a systematic effect in the CO_2 percent error and fit RMS due to changing the degree of the continuum polynomial from poly2 → poly3, which was not seen for CO in Figure 3-6. HITRAN 2020 water spectroscopy is optimal, as seen for CO in Figure 3-7.

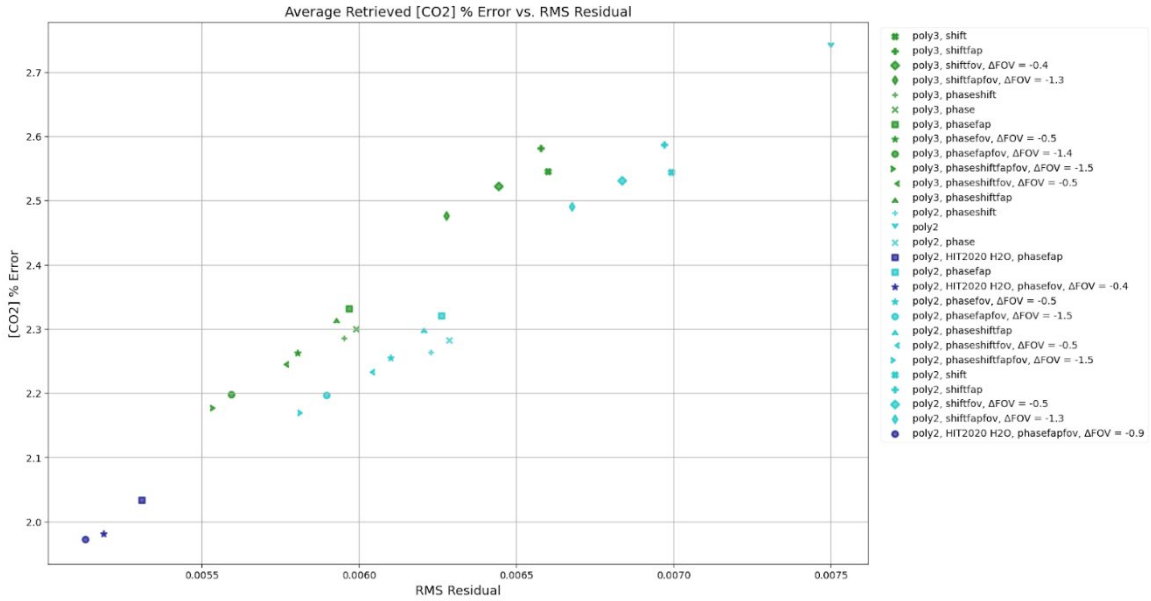

Figure A-14: [CO_2] % Error vs. RMS.

Figure A-15 shows the sensitivity of retrieved [CO_2] to the parameters fitted. A ~10 ppm difference is introduced simply from changing poly3 → poly2 for continuum fitting. Finally, Figure A-16 was created to determine how different each of these results are when considering the retrieval error from MALT. Figure A-15 shows that they all overlap within the MALT error, as in Figure A-13.

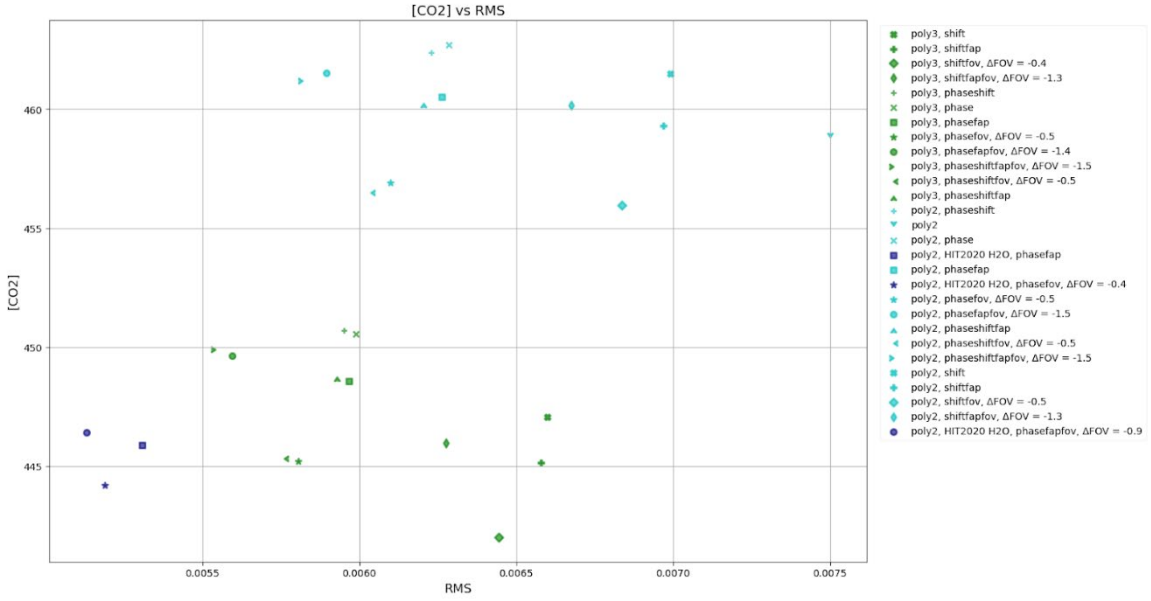

Figure A-15: [CO_2] vs. RMS.

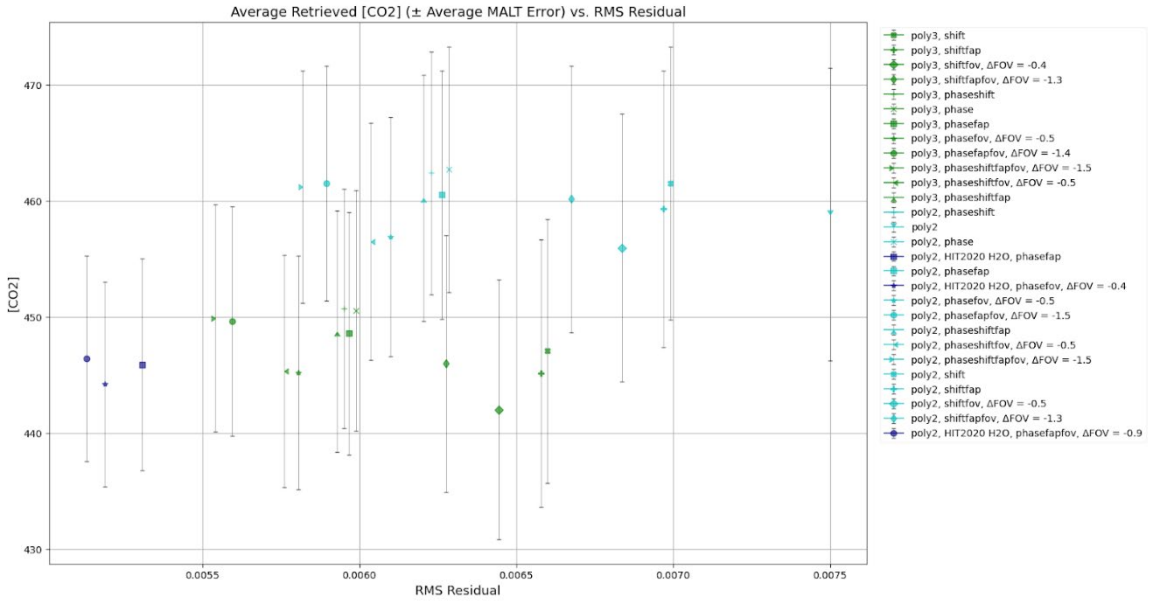

Figure A-16: [CO_2] vs. RMS, MALT error as error bars.

A.4 – CH_3OH Diagnostics

Since this retrieval was mainly relevant for the identification of ship plumes, the diagnostics for the retrieval are stored here instead of section 3.3.

Table A-3: Diagnostics for the Methanol (CH_3OH) retrieval. Fitted on 2021 data from 08/07 – 09/10 and filtered as described in section 2.2. N = 9579 spectra for series 2 and 9575 for series 1.

Average [CH_3OH]	S1: 2.29 ppb S2: 2.32 ppb
Average [CH_3OH] std deviation	S1: 1.44 S2: 1.29
Average % Error from MALT on [CH_3OH]	S1: 58.7% S2: 49.7%
Average RMS	S1: 0.00219 S2: 0.00151
Fitted FOV Value	S1: 24.6 ± 1.4 S2: 25.0 ± 0.6

A.5 – Average Correlation Matrices

An output from each MALT spectral retrieval is a matrix that shows the correlations between each fitted parameter, derived from the algorithm itself. To get a sense of the interplay between fitted parameters over an entire retrieval ensemble, it is useful to create an average correlation matrix. Average correlation matrices for each of the retrievals discussed in this work are presented below, with figure captions indicating the relevant retrieval. For ease of reading, only the matrices for the series 2 retrievals (averaged over 9579 spectra measured between 08/07 and 09/10, 2021) are recorded here.

A.5.1 – CO (and CO_2) Retrieval Average Correlation Matrices

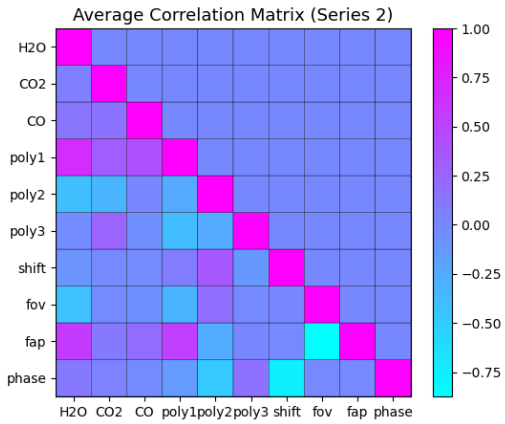

Figure A-17: CO (FAP and FOV fitted) retrieval.

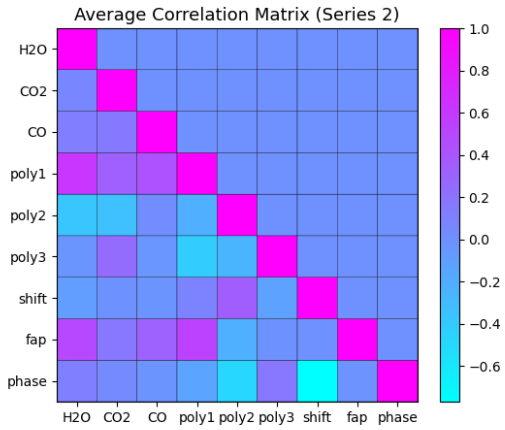

Figure A-18: CO (FAP fitted) retrieval.

A.5.2 – NH_3 Retrieval Average Correlation Matrices

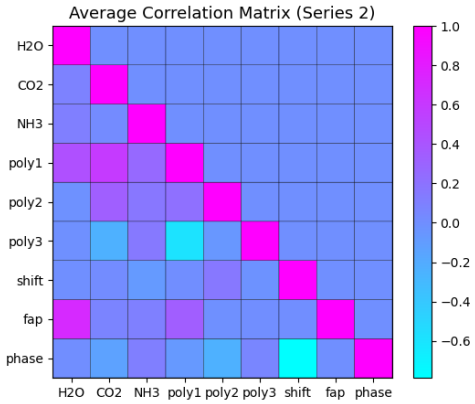

Figure A-19: NH_3 FOV from CO (fixed FOV) retrieval.

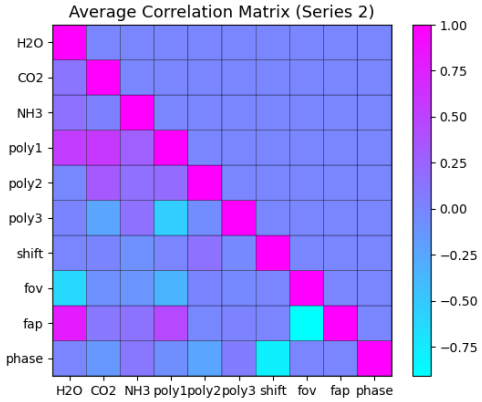

Figure A-20: NH_3 FAP and FOV (FOV initialized at 21.739 mrad – theoretical value) fitted retrieval.

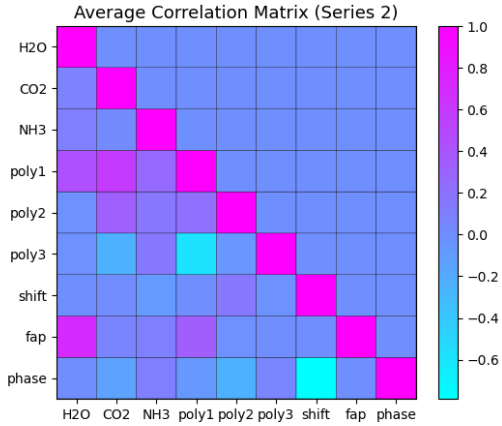

Figure A-21: NH_3 FAP (FOV fixed at 21.739 mrad – theoretical value) fitted retrieval.

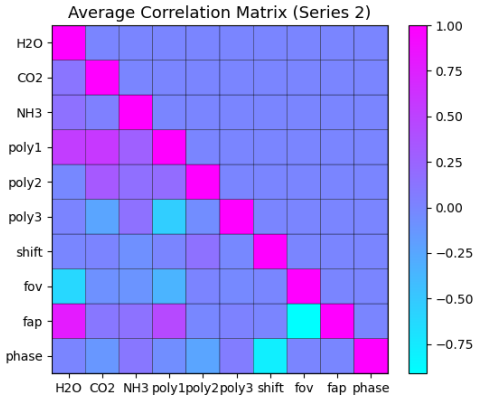

Figure A-22: NH_3 FAP and FOV (FOV initialized at 20.2 mrad – CO retrieval average value) fitted retrieval.

A.5.3 – Other Retrieval Average Correlation Matrices

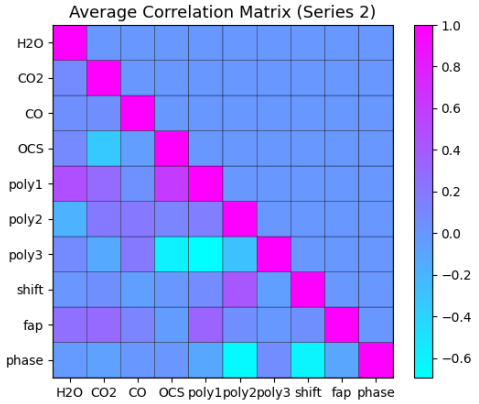

Figure A-23: OCS retrieval average correlation matrix.

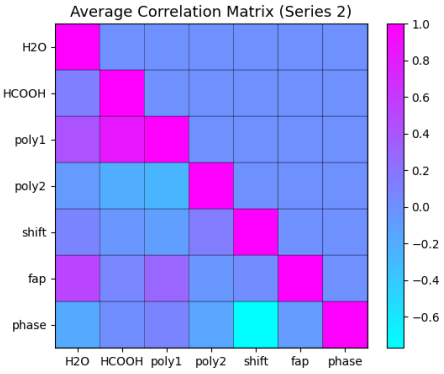

Figure A-24: HCOOH retrieval average correlation matrix.

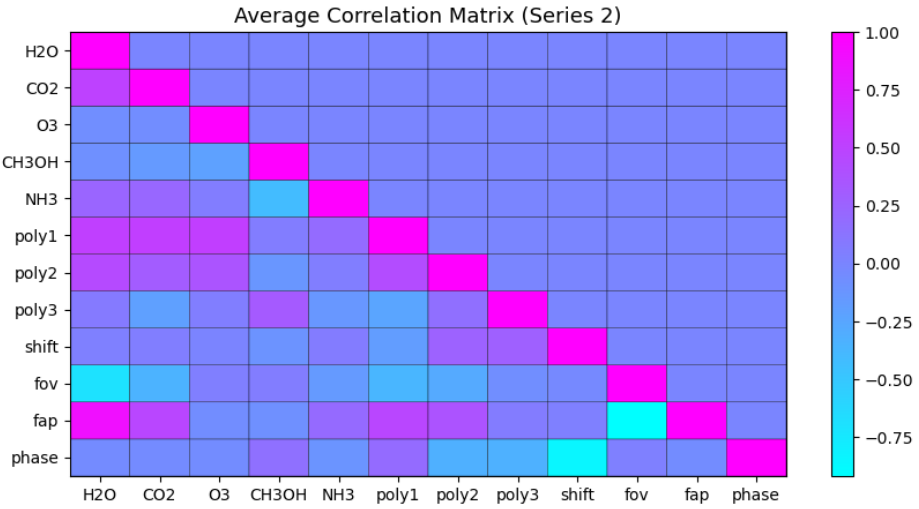

Figure A-25: CH_3OH and O_3 retrieval average correlation matrix.

A.6 – CO_2 Inter-window Comparison

For an idea of how the retrieved CO_2 concentration varies between spectral windows and parameter choices, the time series of CO_2 from each window used in this thesis that included CO_2 as an interfering gas was plotted on the same axis (Figure A-26). This shows that CO_2 is retrieved with a ~10% lower concentration from the inferior (i.e.,

for CO_2 fitting) CH_3OH and NH_3 windows. Although the CH_3OH and NH_3 windows (near 1000 cm^{-1}) have decent CO_2 features, the absorption of these features is < 6%, while in the CO and OCS windows the CO_2 absorption reaches ~20% and 25%, respectively (see Appendix – A.1 for reference). Figure A-27 shows the concentration difference of CO_2 as derived from each of these different retrievals and demonstrates how much more precise the results from the CO and OCS retrievals are. The concentration differences from CO and OCS are much less noisy than the other CO_2 results, and one can see that there is well-defined variation and a promising amount of information in Figure A-28, which even suggests that the CO_2 result from the OCS window is superior because it is more 'repeatable', or precise. This is not a surprise, since the spectral CO_2 absorption feature in the OCS window contains more information as discussed in section 4.2, while at the same time the SNR is higher near 2000 cm^{-1} than near 1000 cm^{-1}.

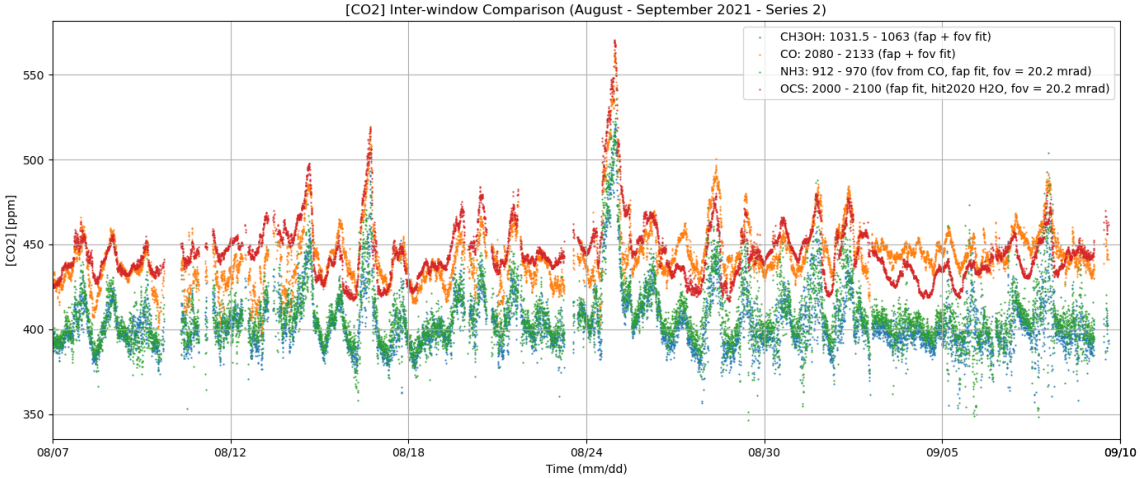

Figure A-26: CO_2 concentration between 08/07 and 09/10, 2021, as retrieved from series 2 data (N = 9579) from each of the windows used in this work that fitted CO_2. The respective retrieval is indicated by the legend.

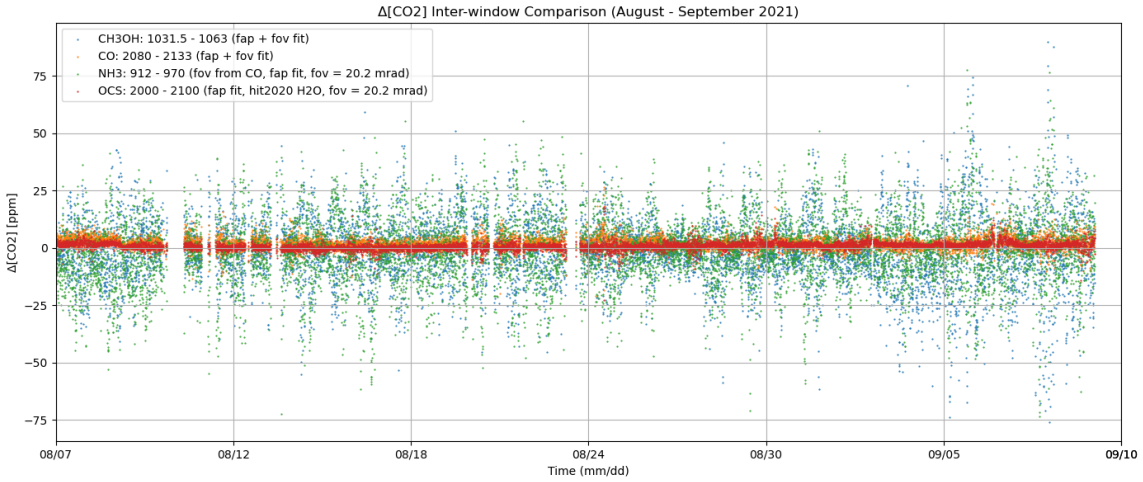

Figure A-27: As for Figure A-26 but showing the CO_2 concentration difference (series 2 - series 1).

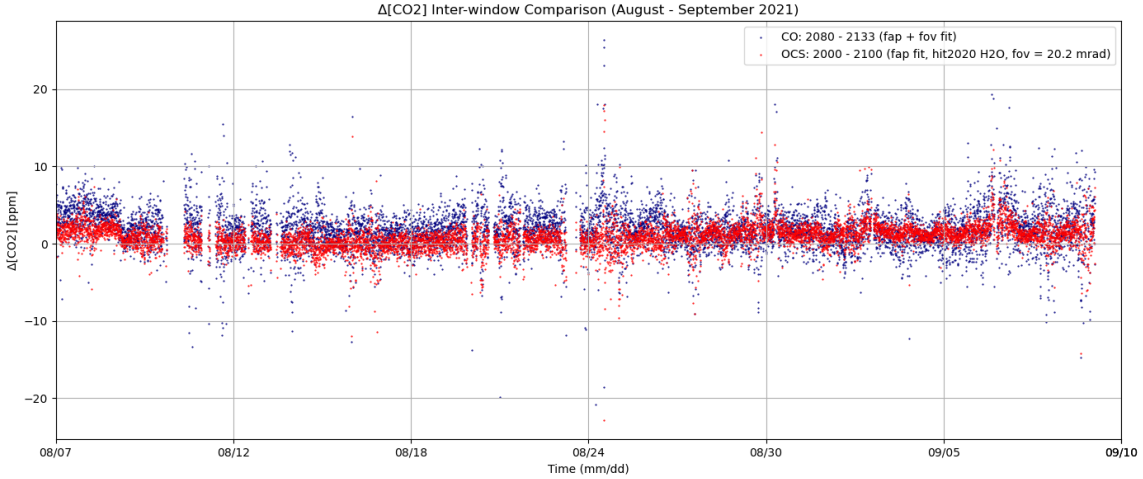

Figure A-28: As for Figure A-27, but only showing the two most precise results; the CO and OCS retrievals.

References

Banwell, C. N., & McCash, E. M. (1994). *Fundamentals of molecular spectroscopy (4th ed.)*. McGraw-Hill.

Behera, S. N., Sharma, M., Aneja, V. P., Balasubramanian, R. (2013). Ammonia in the atmosphere: a review on emission sources, atmospheric chemistry and deposition on terrestrial bodies. *Environmental Science and Pollution Research, 20,* 8092-8131. https://doi.org/10.1007/s11356-013-2051-9

Commane, R., Herndon, S. C., Zahniser, M. S., Lerner, B. M., McManus, J. B., Munger, J. W., Nelson, D. D., & Wofsy, S. C. (2013). Carbonyl sulfide in the planetary boundary layer: Coastal and continental influences. *JGR Atmospheres, 118(14),* 8001-8009. https://doi.org/10.1002/jgrd.50581

Ferek, R.J., & Andreae, M. O. (1984). Photochemical production of carbonyl sulphide in marine surface waters. *Nature, 307*, 148–150. https://doi.org/10.1038/307148a0

Flesch, T. K., Baron, V. S., Wilson, J. D., Griffith, D. W. T., Basarab, J. A., & Carlson, P. J. (2016). Agricultural gas emissions during the spring thaw: Applying a new measurement technique. *Agricultural and Forest Meteorology, 221,* 111-121. https://doi.org/10.1016/j.agrformet.2016.02.010

Flesch, T. K., Prueger, J. H., & Hatfield, J. L. (2002). Turbulent Schmidt number from a tracer experiment. *Agricultural and Forest Meteorology, 3(4)*, 299-307. https://doi.org/10.1016/S0168-1923(02)00025-4

Griffith, D. W. T. (1996). Synthetic Calibration and Quantitative Analysis of Gas-Phase FT-IR Spectra. *Applied Spectroscopy*, *50(1)*. https://doi.org/10.1366/0003702963906627

Griffith, D. W. T. (2010). Computational retrieval of trace gas concentrations from FTIR spectra. *Unpublished manuscript.* David Griffith, Oct 2010

Hannigan, J. & Drews, C. (2023, July 24). SFIT Version 1.0.xx Release. https://wiki.ucar.edu/display/sfit4/SFIT4+Version+1.0.xx+Release

Hellmich, M. (2022). *Ocean-air N2O trace gas fluxes in Halifax Harbour derived from Open-Path FTIR measurements* (Master's thesis, SMU, Halifax, CA). Retrieved from https://library2.smu.ca/bitstream/handle/01/31051/Hellmich_Martin_MASTERS_2022.pdf?sequence=1&isAllowed=y

Kettle, A. J., Rhee, T. S., von Hobe, M., Poulton, A., Aiken, J., & Andreae, M. O. (2001). Assessing the flux of different volatile sulfur gases from the ocean to the atmosphere. *Journal of Geophysical Research, 106(D11),* 12193-12209. https://doi.org/10.1029/2000JD900630

Lennartz, S. T., Marandino, C. A., von Hobe, M., Andreae, M. O., Aranami, K., Atlas, E., Berkelhammer, M., Bingemer, H., Booge, D., Cutter, G., Cortes, P., Kremser, S., Law, C. S., Marriner, A., Simó, R., Quack, B., Uher, G., Xie, H., & Xu, X. (2020). Marine carbonyl sulfide (OCS) and carbon disulfide (CS2): a compilation of measurements in seawater and the marine boundary layer. *Earth System Science Data (ESSD), 12(1),* 591-609. https://doi.org/10.5194/essd-12-591-2020

Miller, S. D., Marandino, C., Saltzman, E. S. (2010). Ship-based measurement of air-sea CO2 exchange by eddy covariance. *JGR Atmospheres, 115(D2)*. https://doi.org/10.1029/2009JD012193

Millet, D. B., Baasandorj, M., Farmer, D. K., Thornton, J. A., Baumann, K., Brophy, P., Chaliyakunnel, S., de Gouw, J. A., Graus, M., Hu, L., Koss, A., Lee, B. H., Lopez-Hilfiker, F. D., Neuman, J. A., Paulot, F., Peischl, J., Pollack, I. B., Ryerson, T. B., Warneke, C., Williams, B. J., & Xu, J. (2015). A large and ubiquitous source of atmospheric formic acid. *Atmospheric Chemistry and Physics, 15*, 6283–6304. https://doi.org/10.5194/acp-15-6283-2015

National Oceanic and Admospheric Administration (NOAA) (2000). *CO2 Flux Map*. PMEL Carbon Program. https://www.pmel.noaa.gov/CO2/file/CO2+Flux+Map

Paulot, F., Jacob, D. J., Johnson, M. T., Bell, T. G., Baker, A. R., Keene, W. C., Lima, I. D., Doney, S. C., & Stock, C. A. (2015). Global oceanic emission of ammonia: Constraints from seawater and atmospheric observations. *Global Biogeochemical Cycles, 29(8),* 1165-1178. https://doi.org/10.1002/2015GB005106

Rothman, L. S., Jacquemart, D., Barbe, A., Chris Benner, D., Birk, M., Brown, L. R., Carleer, M. R., Chackerian, C., Chance, K., Coudert, L. H., Dana, V., Devi, V. M., Flaud, J. -M., Gamache, R. R., Goldman, A., Hartmann, J. -M., Jucks, K. W., Maki, A. G., Mandin, J. -Y., Massie, S. T., Orphal, J., Perrin, A., Rinsland, C. P., Smith, M. A. H., Tennyson, J., Tolchenov, R. N., Toth, R. A., Vander Auwera, J., Varanasi, P., Wagner, G. (2005). The *HITRAN* 2004 molecular spectroscopic database. *Journal of Quantitative Spectroscopy and Radiative Transfer, 96(2)*, 139-204. https://doi.org/10.1016/j.jqsrt.2004.10.008

Sharpe, S.W., Johnson, T. J., Sams, R. L., Chu, P. M., Rhoderick, G.C., & Johnson, P.A. (2004). Gas-phase databases for quantitative infrared spectroscopy. *Appl Spectrosc, 58(12)*, 1452-61. https://doi.org/10.1366/0003702042641281

Smith, T. E. L., Wooster, M. J., Tattaris, M., & Griffith, D. W. T. (2011). Absolute accuracy and sensitivity analysis of OP-FTIR retrievals of CO2, CH4 and CO over

concentrations representative of "clean air" and "polluted plumes". *Atmospheric Measurement Techniques, 4(1),* 97-116. https://doi.org/10.5194/amt-4-97-2011

Watson, A. J., Schuster, U., Shutler, J. D., Holding, T., Ashton, I. G. C., Landschützer, P., Woolf, D. K., & Goddijn-Murphy, L. (2020). Revised estimates of ocean-atmosphere flux are consistent with ocean carbon inventory. *Nature Communications, 11(4422)*. https://doi.org/10.1038/s41467-020-18203-3

Wiacek, A., Li, L., Tobin, K., & Mitchell, M. (2018). Characterization of trace gas emissions at an intermediate port. *Atmospheric Chemistry and Physics, 18(19),* 13787–13812. https://doi.org/10.5194/acp-18-13787-2018